AD-A101 074   CASE WESTERN RESERVE UNIV CLEVELAND OHIO DEPT OF MET--ETC F/G 11/2
OXIDATION OF NON-OXIDE CERAMICS.(U)
JUN 81   T E MITCHELL, R M CANNON   F49620-78-C-0053
UNCLASSIFIED   AFOSR-TR-81-0530   NL

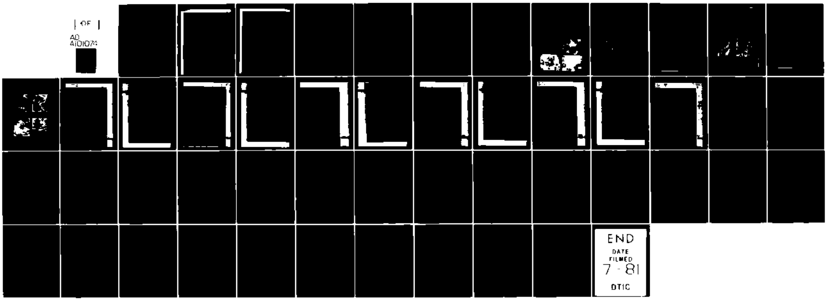
1 OF 1
AD
A101074
END
DATE
FILMED
7-81
DTIC

5C AFOSR-TR- 81-0530
14

(12)

LEVEL

Interim Scientific Report On

6 OXIDATION OF NON-OXIDE CERAMICS

submitted to the Air Force Office of Scientific Research

15
Contract F49620-78-C-0053 16

~~for the period~~ Apr[redacted]80 — Apr[redacted] [redacted]981

by

10 T. E. Mitchell, R. M. Cannon, D. M. Mieskowski
N. J. Tighe [redacted] A. H. Heuer

Depar~~tment~~ of Metallurgy and Materials Science
Case Western Reserve Univ~~ersity~~
Cleveland, Oh~~io~~ 44106

9) 50

AD A101074

DTIC FILE COPY

DTIC
ELECTE
JUL 7 1981
C

Approved for public release;
distribution unlimited.

81 7 06 024

Unclassified

SECURITY CLASSIFICATION OF THIS PAGE (When Data Entered)

REPORT DOCUMENTATION PAGE

READ INSTRUCTIONS BEFORE COMPLETING FORM

1. REPORT NUMBER: **AFOSR-TR- 81 -0530**

2. GOVT ACCESSION NO.: AD-A101 074

3. RECIPIENT'S CATALOG NUMBER

4. TITLE (and Subtitle)
OXIDATION OF NON-OXIDE CERAMICS

5. TYPE OF REPORT & PERIOD COVERED
Annual Report
April 1980 - April 1981

6. PERFORMING ORG. REPORT NUMBER

7. AUTHOR(s)
T.E. Mitchell, R.M. Cannon, D.M. Mieskowski,
N.J. Tighe and A.H. Hener

8. CONTRACT OR GRANT NUMBER(s)
F49620-78-C-0053

9. PERFORMING ORGANIZATION NAME AND ADDRESS
Case Western Reserve University
Cleveland, OH 44106

10. PROGRAM ELEMENT, PROJECT, TASK AREA & WORK UNIT NUMBERS
2306/A2 61102F

11. CONTROLLING OFFICE NAME AND ADDRESS
AFOSR/NE
Bolling AFB, D.C. 20332

12. REPORT DATE
12 June 81

13. NUMBER OF PAGES
48

14. MONITORING AGENCY NAME & ADDRESS (if different from Controlling Office)

15. SECURITY CLASS. (of this report)
Unclassified

15a. DECLASSIFICATION/DOWNGRADING SCHEDULE

16. DISTRIBUTION STATEMENT (of this Report)
Approved for public release; distribution unlimited.

17. DISTRIBUTION STATEMENT (of the abstract entered in Block 20, if different from Report)

18. SUPPLEMENTARY NOTES

19. KEY WORDS (Continue on reverse side if necessary and identify by block number)
Silicon Carbide, Sintering, In-sita Oxidated, YTTRIA-doped siliconnitride

20. ABSTRACT (Continue on reverse side if necessary and identify by block number)
Tracer studies involving CVD single crystals oxidized in oxygen 16 and oxygen 18 were unsuccessful in indicating the direction of diffusing species during oxidation of SiC. A refinement of this technique is planned. Research is also continuing on the characterization of the spherulitic growth which appears during oxidation...The influence on densification of pore curvature, dihedral angle, applied stress and internal pore pressure was undertaken from a theoretical point of view. The results using a simple model indicate that at low dihed-

DD FORM 1 JAN 73 1473 EDITION OF 1 NOV 65 IS OBSOLETE

Unclassified

SECURITY CLASSIFICATION OF THIS PAGE (When Data Entered) ral angle (less than 60 degrees) there is an equilibrium porosity in a poly-crystalline material; for such a material there is no barrier to nucleation of cavities in dense material. At intermediate dihedral angles, pores with few sides would shrink and disappear, whereas those with many sides would initially shrink but would reach an equilibrium size at which densification would stop. In this case grain growth of the large pores would reduce the number of sides for the pore and promote further densification. For such materials there would be a small barrier to nucleation.

1. Introduction

This report describes progress which has been made during the last year on oxidation and sintering of non-oxide ceramics. A number of personnel activities occurred in this period. Ms. Monaghan who joined us in August, 1979 from Birmingham University to work on the oxidation of Si_3N_4 departed in the Summer of 1980. Ms. Mieskowski joined us in January 1980 from Penn State University via Union Carbide and continues to work on oxidation of SiC and will soon write her M.S. thesis. Prof. Cannon spent January to June 1980 on sabbatical leave from MIT to do theoretical work on sintering of non-oxide ceramics in cooperation not only with us, but also with Prof. Moller who had been on leave from the University of Gottingen working on grain boundaries and sintering of silicon. Prof. Moller has since left but stays in contact. Dr. Tighe has continued to visit from NBS to perform oxidation experiments on Si_3N_4 using the environmental cell of the high voltage electron microscope (HVEM).

2. Oxidation of SiC

During the past 20 years, a number of investigations concerning the mechanism of SiC oxidation have been conducted. In general, these studies have supported the idea that oxidation occurs by the inward diffusion of some species of oxygen through the SiO_2scale. The initial work on this contract raised the question of whether this concept was in error based on observations of spherulitic crystallization of the amorphous SiO_2scale (See our publication in Appendix 1).

Spherulites in oxide scales <1 μm in thickness are actually disc-shaped rather than spheriodal. They have been observed on all of the samples tested to date which have included CVD and Acheson-type single crystals and α and β polycrystalline SiC. However, growth of additional layers of spherulites on top of previously existing ones was not apparent in any of these experiments.

A tracer study involving CVD single crystals oxidized both in ^{16}O and ^{18}O was performed but was unsuccessful in indicating the direction of the diffusing species. The samples had been oxidized as received instead of being polished sufficiently to assure a flat surface: data interpretation was impossible because of the crystal growth steps. The experiment will be repeated but with specimens of α and β polycrystalline SiC which have already been polished and oxidized in ^{16}O.

An experiment is also being planned which will provide information on the effect of cleanliness of spherulitic growth. All specimens to date have been cleaned with dilute HF, distilled H_2O, and ethanol under open laboratory conditions and oxidized in furnaces which are used for various types of controlled atmospheric work. Selected specimens will be prepared in the "clean room" used for microelectronics research and then oxidized in an adjacent area. These will then be examined and compared to previously oxidized samples.

The following table is a summary of recent oxidations and microscopy:

Single crystals

Temp.	Time	P_{O_2}	SiC type	microscopy
1300°C	1,2,5,10,20 40,60 hrs.	ambient	CVD, Acheson (also single crystal Si)	optical
1350°C	1,2,3,5,10, 20 hrs.	1 atm	CVD, Acheson	"
1400°C	88 hrs.	ambient	CVD, Acheson	TEM

AIR FORCE OFFICE OF SCIENTIFIC RESEARCH (AFSC)
NOTICE OF TRANSMITTAL TO DDC
This technical report has been reviewed and is
approved for public release IAW AFR 190-12 (7b).
Distribution is unlimited.
A. D. BLOSE
Technical Information Officer

Accession For
NTIS GRA&I ✓
DTIC TAB
Unannounced
Justification
By
Distribution/
Availability Codes
Avail and/or
Dist Special
A

Polycrystalline SiC

Temp.	Time	Thickness	P_{O_2}	SiC type	microscopy
1200°C	*	∿0.25,0.50 1.0μm	1 atm	α,β	optical, SEM
1300°C	*	∿0.25,0.50 1.0μm	"	"	optical, SEM, TEM
1350°C	28,32, 128 hrs.	*	ambient	"	optical
1400°C	*	∿0.25,0.50 1.0	1 atm	"	optical, SEM

* not a primary consideration

The SEM examination of oxidized α and β polycrystalline SiC revealed bubbles which may be attributed to CO, and perhaps SiO, formation at the substrate/scale interface. EDAX will be used to check bubble composition.

TEM studies have centered on spherulite morphology and the associated defect structure. The spherlite are found to be heavily faulted and twinned, due to the β → α cristobalite transformation. EDAX will be used to determine the extent of impurity atom/ion migration to the spherulite grain boundaries.

3. Oxidation of Si_3N_4

The basis of this work is given in Appendix 2, which is a reprint of our work published in Electron Microscopy 1980. We are continuing to co-operate with Dr. Tighe to use the HVEM environmental cell and analytical electron microscopy techniques to understand the catastrophic oxidation of Y_2O_3-doped Si_3N_4. This work has been quiescent since Ms. Monaghan left but will pick up now that H. C. Liu (who has just finished his Ph.D. with Prof. Mitchell) has agreed to stay on and do this research.

4. Sintering of Covalent Solids.

Two aspects of sintering have been considered from a theoretical point of view. One is on the structure of grain boundaries in covalent solids using the coincidence site lattice model as applied to Si. This work was done by Dr. Moller during his stay here and the published paper is given in Appendix 3. The other area is on the influence of pore curvature, dihedral angle, applied stress and internal pore pressure on densification, in an attempt to understand the poor sinterability of covalent solids. This work was undertaken in co-operation with Professor Cannon during his Sabbatical leave here last year and the first draft of a paper is given in Appendix 4.

5. Other Research.

Several other papers have been published over the past year resulting from AFOSR-sponsored research. These include:

(a) A.H.Heuer, L.U.Ogbuji and T.E.Mitchell, "High Resolution Studies of the Final Stages of the $\beta \rightarrow \alpha$ Transformation in Polycrystalline SiC", in "Electron Microscopy and Analysis 1979", (Inst. of Physics, London), p. 453 (1979).

(b) L.U.Ogbuji, T.E.Mitchell and A.H.Heuer, "The $\beta \rightarrow \alpha$ Transformation in Polycrystalline SiC: III, The Thickening of α Plates", J. Amer. Ceram. Soc., 64, 91 (1981).

(c) L.U.Ogbuji, T.E.Mitchell, A.H.Heuer and S. Shinozaki, "The $\beta \rightarrow \alpha$ Transformation in Polycrystalline SiC: IV, A Comparison of Conventionally Sintered, Hot-Pressed, Reaction-Sintered, and Chemically Vapor-Deposited Samples", J. Amer. Ceram. Soc., 64, 100 (1981).

Reprinted from the Journal of The American Ceramic Society, Vol. 63, No. 5–6 May-June, 1980
Copyright 1980 by The American Ceramic Society

The Microstructure of Oxide Scales on Oxidized Si and SiC Single Crystals

A. H. HEUER,[*] L. U. OGBUJI,[*] and T. E. MITCHELL[*]

THE first oxidation product of both Si and SiC is amorphous SiO_2, which devitrifies to cristobalite during growth of the scale. The present note describes preliminary studies of oxidation of single crystals in unmodified laboratory ambients, at 1100° to 1250° for Si and 1350° to 1500°C for SiC; the cristobalite invariably crystallizes with a spherulitic morphology. The initially formed spherulites provide a convenient marker for ascertaining whether oxidation occurs at the substrate-SiO_2 or the SiO_2-gas interface. The Si and SiC single crystals differ most significantly in this regard: in SiC, after the first layer of spherulites forms, subsequent spherulites form on *top* of the previous layer; in Si the initial appearance of the first layer remains unchanged with further oxidation, suggesting that subsequent oxide forms *beneath* the first layer.

Various grades of α-SiC single crystals were investigated, ranging from a relatively impure, commercial-grade material,[*] through variously doped samples to colorless, semiconductor-grade material.[†] The B-doped Si samples were also of semiconductor grade.[‡] Both materials were sectioned along their close-packed planes ((0001) for SiC, {111} for Si), polished, and oxidized for various times in the laboratory ambient. The results shown here are from SiC samples oxidized at 1400° and Si samples oxidized at 1250°C, but are typical of all the samples investigated. The structure of the oxide scale was identified by X-ray and electron diffraction and its morphology was determined by optical and transmission electron microscopy (TEM). All scales studied gave rise to interference colors, from which we infer a scale thickness $\leq 1\ \mu m$; the spherulites are thus actually disks which are quite thin compared to their diameters ($\approx 100\ \mu m$).

Figure 1 is an optical micrograph of cristobalite spherulites on SiC after oxidation for 12 h at 1400°C, showing that smaller spherulites grow on top of the larger ones. The sequence of such growth is illustrated in Fig. 2. Figure 2(*A*) shows the initial layer of spherulites formed after 1 h at 1400°C; additional oxidation for 11 h produced the second generation of finer spherulites evident in Fig. 2(*B*). The result of a similar, sequential oxidation experiment on Si at 1250°C is shown in Fig. 3, where Fig. 3(*A*) shows the structure after 20 h, whereas Fig. 3(*B*) shows the same region of scale after 52 h. The gross surface appearance of the oxide scale on Si did not change with oxidation time; TEM investigation showed that the change in the apparent "texture" of the spherulites on Si involved reduction of the amount of residual glass within the spherulites and coarsening of their constituent cristobalite microcrystals.

Two basic kinetic questions with respect to the mechanism of oxidation of these materials are of interest: first, whether oxidation occurs by inward diffusion of oxygen and reaction at the substrate/SiO_2 interface (with subsequent outward diffusion of CO or some other carbonaceous species in the case of SiC) or by outward diffusion of Si in the case of Si and Si and C (or SiO and CO) in the case of SiC and reaction at the SiO_2/air interface and, second, whether the rate-controlling process is inward diffusion, outward diffusion, or an interface-reaction mechanism. The microstructural evolution of the oxide scale on Si suggests that oxygen diffuses through the oxide scale to react at the Si/SiO_2 interface, a point of view consistent with the previous literature on oxidation of Si.[1,2]

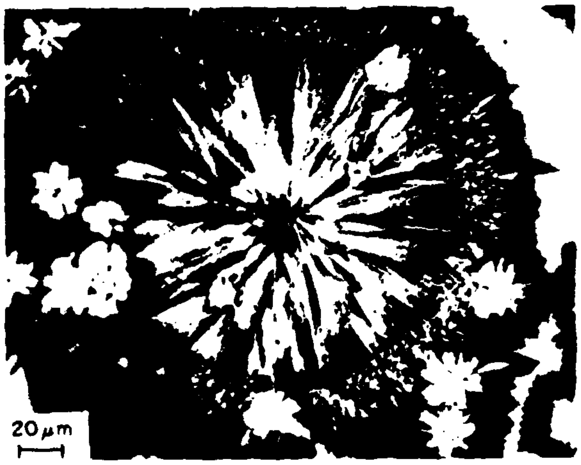

Fig. 1. Optical micrograph of spherulitic cristobalite scale on SiC oxidized for 12 h at 1400°C.

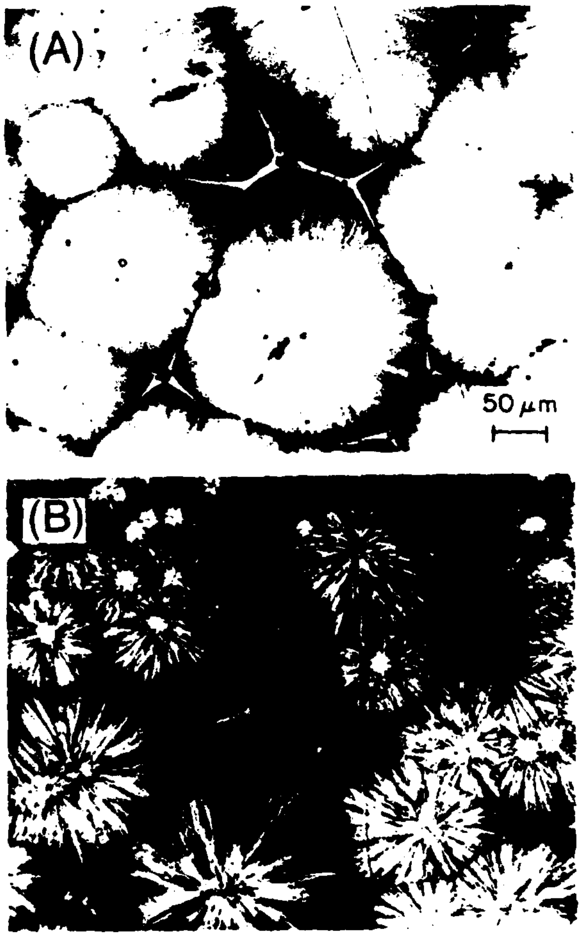

Fig. 2. Optical micrographs of spherulitic cristobalite scale of SiC (*A*) oxidized for 1 h at 1400°C and (*B*) further oxidized for 11 h at 1400°.

Presented at the 81st Annual Meeting, The American Ceramic Society, Cincinnati, Ohio, May 2, 1979 (Basic Science Division No. 147-B-79). Received December 3, 1979; revised copy received March 17, 1980

Supported by the Air Force Office of Scientific Research under Contract No. 49620-78C-0053

At the time this work was done, the writers were with the Department of Metallurgy and Materials Science, Case Institute of Technology, Case Western Reserve University, Cleveland, Ohio 44106 L. U. Ogbuji is now with the Department of Materials Science, University of Florida, Gainesville, Florida 32611

[*] Member, the American Ceramic Society

[*] Supplied by Electroschmelzwerke, Munich, Federal Republic of Germany.

[†] Supplied by R. Potter, General Electric Co., Nela Park, Cleveland, Ohio.

[‡] Supplied by N. Shaw, National Aeronautics and Space Administration Lewis Research Lab, Cleveland, Ohio

Our results on SiC suggest strongly, however, that oxidation of this material occurs at the SiO_2/air interface, not at the SiO_2/SiC interface. This outward-growing scale requires that outward transport of Si and C in some form (SiC "molecules," SiO, CO, etc.) be the rate-controlling process during oxidation of SiC. This point of view is contrary to many assertions in the literature which imply that the inward diffusion of oxygen is the rate-controlling process. That the actual rate-controlling process for oxidation of SiC is controversial can be seen from the following:

(*a*) Motzfeldt[3] examined the older data on the oxidation of Si and SiC and concluded that, in both cases, inward diffusion of O_2 is rate-controlling.

(*b*) Jorgensen *et al.*[4] discounted the idea of molecular diffusion of O_2, CO, or CO_2 and suggested that the diffusing species must be O or Si ions.

(*c*) Fitzer and Ebi[5] found that the Arrhenius plot of parabolic oxidation rate had three stages as a function of reciprocal temperature and proposed that the rate-controlling mechanism changes from O_2 diffusion below ≈1400°C to CO diffusion at higher temperatures.

(*d*) Singhal[6] found a very high activation energy for the parabolic oxidation rate (480 kJ/mol vs ≈60 to 280 kJ/mol found by previous investigators) and concluded that desorption of CO from the SiC-SiO_2 interface must be rate-controlling.

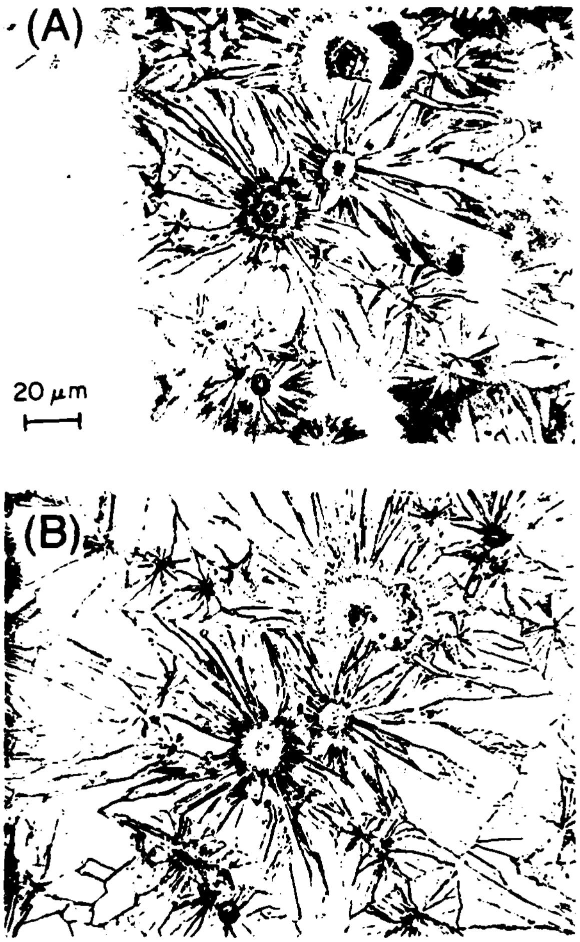

Fig. 3. Spherulitic cristobalite on Si oxidized at 1250°C for (*A*) 20 h and (*B*) 52 h.

None of the previous investigators systematically considered the effects of impurities on the oxidation kinetics, although we have shown[7] that high-temperature annealing of sintered SiC improves the oxidation resistance (presumably by evaporation of the B added as a sintering aid) and it is common knowledge that the oxidation resistance of hot-pressed SiC depends on the type and amount of densification aid added. Furthermore, there has been inadequate consideration given to the effect of devitrification on either the kinetics or mechanism of oxidation. It is thus apparent that the oxidation of SiC is still far from understood, but it appears from the present work that outward diffusion of Si and C is important. It is not certain, however, whether Si or C (or SiO or CO) is the rate-controlling species.

NOTE ADDED IN PROOF: Costello *et al.*[8] recently reported that platinum marker experiments showed that the oxide scale on SiC grew by inward diffusion of oxygen and that the spherulites were nucleated at the SiC surface. Their work thus suggests that the second generation of spherulites observed in our experiments might have occurred by the crystallization of vitreous silica remaining on top of the first generation of spherulites. It is clear that the oxidation of SiC is far from understood; experiments are in progress using isotopic tracers to attempt to resolve some of these points.

---

[1] A. R. Cooper, A. H. Heuer, and L. D. Major, Jr., "Proton Activation Studies of the Thermal Oxidation of Silicon," Air Force Materials Laboratory Tech. Rept. No. AFML-TR-78-119, Aug. 1978.

[2] E. Rosencher, A. Straboni, S. Rigo, and G. Amsel, "An ^{18}O Study of The Thermal Oxidation of Silicon in Oxygen," *Appl. Phys. Lett.*, **34** [4] 254–56 (1979).

[3] K. Motzfeldt, "On the Rates of Oxidation of Silicon and Silicon Carbide in Oxygen, and Correlation with Permeability of Silica Glass," *Acta Chem. Scand.*, **1** [7] 1596–1606 (1964).

[4] P. J. Jorgensen, M. E. Wadsworth, and I. B. Cutler, "Effects of Water Vapor on Oxidation of Silicon Carbide," *J. Am. Ceram. Soc.*, **44** [6] 258–61 (1961).

[5] E. Fitzer and R. Ebi, pp. 320–28 in Silicon Carbide 1973. Edited by R. C. Marshall, J. W. Faust, Jr., and C. E. Ryan. University of South Carolina Press, Columbia, S.C., 1974.

[6] S. C. Singhal, "Oxidation Kinetics of Hot-Pressed Silicon Carbide," *J. Mater. Sci.*, **11** [7] 1246–53 (1976).

[7] L. U. Ogbuji, T. E. Mitchell, and A. H. Heuer, "Microstructure of the Oxidation Product of SiC"; for abstract see *Am. Ceram. Soc. Bull.*, **58** [3] 350 (1979).

[8] J. A. Costello, I. S. T. Tsong, and R. E. Tressler, "Oxidation of SiC"; for abstract see *Am. Ceram. Soc. Bull.*, **58** [3] 356 (1980).

Appendix 2

In Situ Oxidation of Y_2O_3-doped Si_3N_4

N. J. Tighe, National Bureau of Standards
Washington, D. C.

K. Kuroda, T. E. Mitchell and A. H. Heuer
Case Western Reserve University
Cleveland, Ohio

Hot-pressed Si_3N_4+8-13%Y_2O_3 compacts, which exhibited catastrophic oxidation in air at 740°C but only passive oxidation at 1380°C, were studied by HVEM using an environmental cell. The *in situ* experiments were started as part of a larger program to establish a model for this catastrophic oxidation process. The low temperatures required for initiation of oxidation are within the capability of the hot stage and the reaction products are sufficiently complex to require analysis by electron diffraction. This yttria-doped silicon nitride ceramic is of interest for use in ceramic turbine engine components because of its good mechanical properties at temperatures above 1200°C [1]. However, until the cause of the low temperature catastrohpic oxidation is identified and corrected the material cannot be manufactured successfully for these components. The low temperature oxidation is similar in appearance to the so-called "pest condition" and occurs in some billets and not in others which were manufactured under the same apparent commercial, powder processing and hot pressing conditions. Lange *et al.* [2] found that billets they prepared in the Si_3N_4-Si_2N_2O-Y_2[illegible] compatibility triangle of the phase equilibrium diagram, shown in Fig. 1, were oxidation resistant; and, that billets with compositions outside this triangle were unstable in oxidizing conditions.

In this paper, the material designated -A- exhibited only passive oxidation during heating in air from 600°C to 1400°C; while the material designated -B- exhibited catastrophic oxidation during heating in air at 740°C. Both billets are from the same manufacturer [3]. A bar of material -B- when heated in a gradient furnace from 735°C to 1380°C for 20 hours oxidized catastrophically at the low temperature end, and passively at the high temperature end. The major crystalline phases in both materials were identified by powder x-ray diffraction as βSi_3N_4, $Y_{10}Si_7O_{23}N_4$ (H phase) and WSi_2 (there were some unidentified lines). The tungsten phase (3-4%) is a result of contamination from WC balls used in ball-milling of the silicon nitride powder, and thus is a common impurity phase in hot-pressed Si_3N_4. The WSi_2 phase was not present in the catastrophically oxidized portion of the material B, but was present in the portion oxidized at 1380°C. Although the compositions of A and B were similar, there was considerable phase segregation and inhomogeneity in material B as seen in the light microscope. Both materials appear to have compositions outside the compatibility triangle discussed by Lange *et al.* [2].

The Swann environmental cell in the CWRU 650kV electron microscope was used with a platinum strip heater, in flowing oxygen. Specimens of materials -A- and -B- were prepared as ion-thinned discs with one flat side and one dished side. This configuration gave good contact with the grid heater; and, resulted in better heat conduction to the specimen.

The microstructure of the yttria -A- is shown in Fig. 2, and is similar to that found in other billets [4,5]. The large tabular grains are Si_3N_4, the triangular shaped phases surrounding the grain corners are the Y_2O_3 + Si_3N_4 phases and the dark particles along the grain boundaries are the WSi_2 and/or WC phases. During hot-pressing at 1750-1800°C, the yttrium oxynitride phases can melt and form a series of solid solutions with the impurity phases and with the silica in the starting powder [5]. Both crystalline and non-crystalline phases of variable composition can fill the interstices around Si_3N_4 grains.

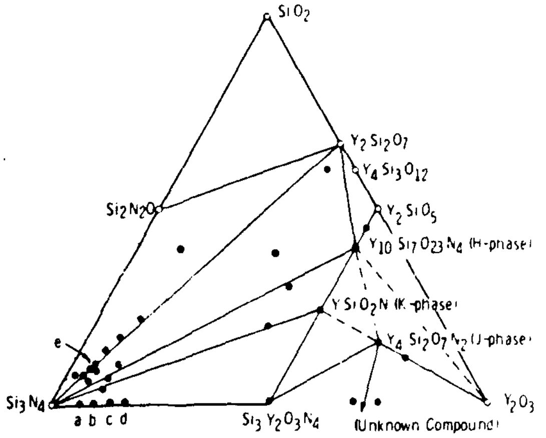
SiO2
Y2Si2O7
Y4Si3O12
Y2SiO5
Si2N2O
Y10Si7O23N4 (H-phase)
YSiO2N (K-phase)
Y4Si2O7N2 (J-phase)
e
Si3N4
a b c d
Si3Y2O3N4
(Unknown Compound)
Y2O3

Fig. 1 Phase diagram for the yttria sialons [1].

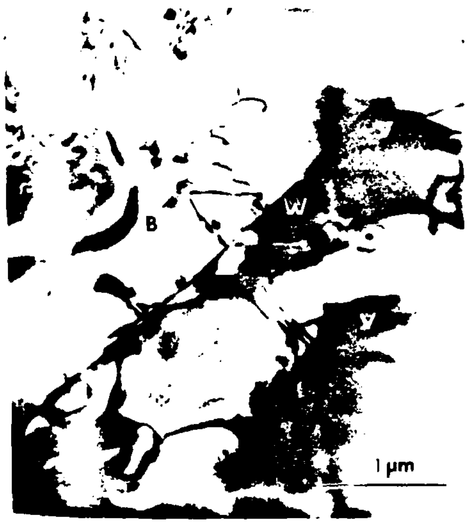

Fig. 2. Microstructure of hot-pressed [illegible]O_3 showing βSi_3N_4 (B), grains [illegible] phase (Y) WSi_2 particles (W).

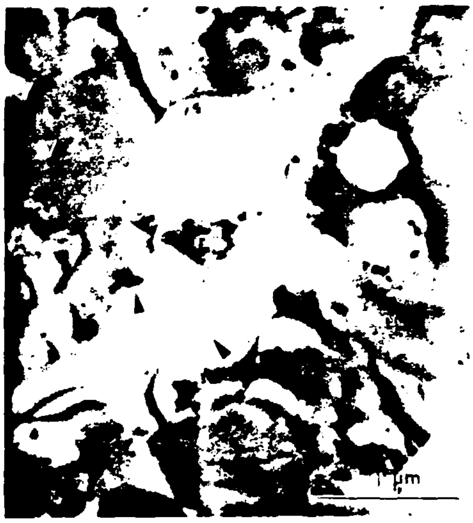

Fig. 3. Material -B- 750°C torr O_2 after heating for ~5 min., showing oxide platelets (arrowed) and reacting yttria phase (Y).

Specimens were heated gradually to 750°C in 40 torr of O_2. Under these conditions oxide platelets were seen to nucleate on the surfaces of the βSi_3N_4 grains, around holes and at the yttria phases as in Fig. 3. The platelets, which were randomly oriented and incoherent with the matrix, gave spotty ring patterns both at temperature and after cooling to room temperature. The platelets in Fig. 4 were identified from these ring patterns as a mixture of SiO_2 and Si_2N_2O. During the oxidation considerable drift and flexure of the specimens occurred, as is evident in the figures.

After a few minutes of heating, cracks appeared along some grain boundaries; then, as oxidation proceeded a film was observed to grow by the merging of nucleating clusters. These clusters changed diffraction contrast as they merged. It is assumed, at this time, that this process represented the gradual reaction and volatization of the tungsten rich phase. The film thickened and the crack widened to form a large hole as seen in Fig. 5. Iron rich and tungsten depleted phases around reacted thin foil edges were detected with an EDX system on a 200 KV instrument [7].

The yttria-silicon oxynitride phases became porous during the *in situ* oxidation. This type of reaction can be seen at Y in Fig. 5 and in Fig. 6. The morphology of the phases suggests that the initial, yttria-rich regions were multiphase or possibly an amorphous-crystalline mixture. The phase in Fig. 6 was identified from its electron diffraction pattern as $YSiO_2N$ or the K-phase of Fig. 1.

The *in situ* specimens were bent and slightly pink when removed from the strip heater. Later TEM examination showed that the oxidation had not occurred uniformly over the entire thin area of the specimens. Some of the differences reflect the temperature gradient present between parts of the specimen that are exposed through holes in the grid heater and other parts of the specimen that were under the grid bars. In the region shown in Fig. 7 few oxide platelets are seen, and the boundaries between Si_3N_4 grains have opened. The yttria phase visible on one edge of the grain was identified as $Y_4Si_2O_7N_2$ or the J phase. The oxidation rate differences could reflect also the inhomogenity of the phase distribution mentioned previously.

Additional *in situ* experiments are needed to verify the mechanism of the loss of W and the observed reaction differences. Video or cine´ recording will be used to make a more complete record of the observations.

The results of the *in situ* experiments demonstrate that: catastrophic low temperature oxidation in yttria-silicon material -B- started at surfaces exposed to oxygen; volatization of a W containing phase created voids; continuous films were produced over some grains; yttria rich phases became porous; and considerable strain was associated with the oxidation.

References

1. G. E. Gazza, J. Amer. Ceram. Soc. 56, 662 (1973).
2. F. F. Lange, S. C. Singhal and R. C. Kuznicki, Westinghouse Report 76-904 (1976).
3. The Norton Co. Material Designation NCX-34.
4. D. R. Clarke and G. Thomas, J. Amer. Ceram. Soc. 60 491-5 (1977).
5. O. L. Krivanek, T. M. Shaw and G. Thomas, J. Amer. Ceram. Soc., 62, 585-[illegible] (1979).
6. K. H. Jack in Nitrogen Ceramics, F. L. Riley ed. Noordhoff, 1977, p. 109-125.
7. G. Nord, USGS, Reston, Va.

This work is supported partially by DOE Office of Coal Utilization under Task Order No. A0861FC and by AFOSR grant 49620-78C-0053. The material -B- was supplied by J. Wimmer of Garrett AiResearch, Phoenix, Az.

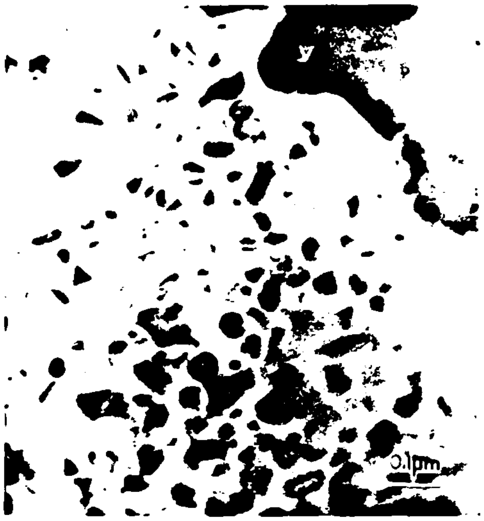

Fig. 4. βSi_3N_4 grain with SiO_2 and Si_2N_2 platelets produced during *in situ* oxidation. Yttria phase at Y.

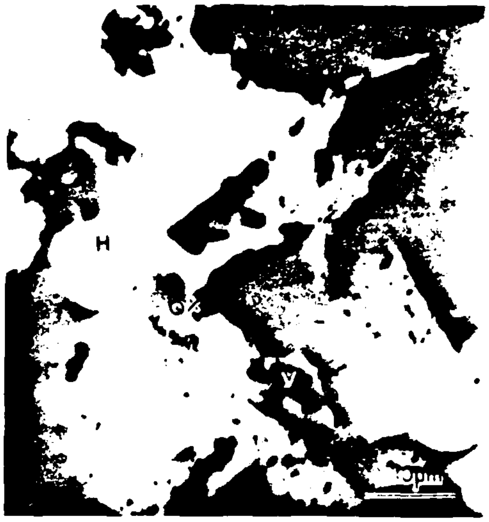

Fig. 5. Specimen at 750°C in Torr O_2. The hole (H) and the film around it (Ox) were produced in ∿30 min.

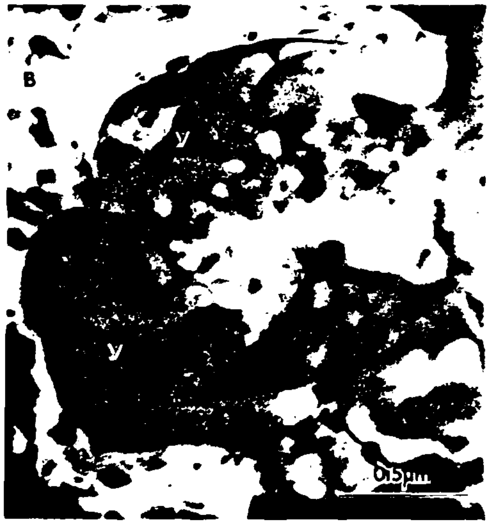

Fig. 6. Material -B-. After oxidation the yttria phase (Y) is porous and layered, βSi_3N_4 grains (B) have oxide platelets.

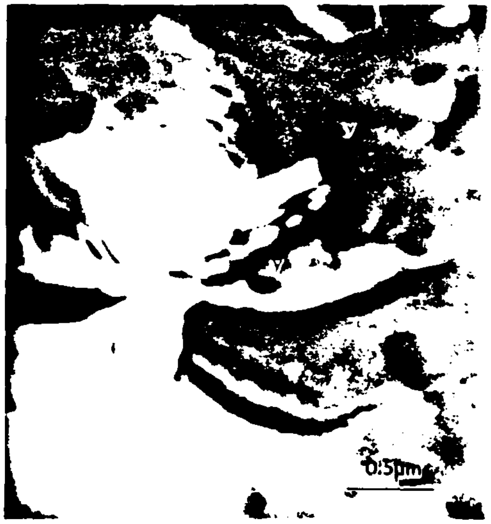

Fig. 7. Portion of *in situ* specimen which was under the grid, yttria phase (Y) is $Y_4Si_2O_7N_2$.

Appendix 3

PHILOSOPHICAL MAGAZINE A, 1981, VOL. 43, NO. 4, 1045–1055

⟨011⟩ tilt boundaries in the diamond cubic lattice

By H.-J. MÖLLER†
Department of Metallurgy and Materials Science, Case Western Reserve University, Cleveland, Ohio 44106, U.S.A.

[Received 7 February 1980 and accepted 18 June 1980]

ABSTRACT

The application of the coincidence site lattice (CSL) model to the diamond cubic structure allows a purely geometric modelling of specific grain boundaries. Symmetric ⟨011⟩ CSL tilt boundaries with $\Sigma \leqslant 33$ were constructed with energies lower than the energy of a random boundary. Structures without broken bonds were found for rotation angles $\theta \leqslant 70{\cdot}53°$. Boundaries within the range $\theta \leqslant 26{\cdot}53°$ ($\Sigma = 19$) are considered as small-angle boundaries consisting of an array of edge dislocations.

§ 1. INTRODUCTION

There is considerable interest in the use of polycrystalline semiconductors for solar cells and thin-film devices, and the investigation of the electrical properties of their grain boundaries is of increasing importance. One of the basic objectives of this study is the determination of the atomic structure of arbitrary high-angle grain boundaries. Much progress in the investigation of grain boundaries has already been achieved in f.c.c. metals, but only a few results were obtained in covalently bonded crystals (Hornstra 1959, 1960, Kohn 1958, Holt 1964, Krivanek, Isoda and Kobayashi 1977). It is the purpose of this paper to resume these investigations in the diamond cubic structure from a more general approach.

Experimental evidence exists for f.c.c. metals that the structure of arbitrary boundaries can be developed from a few low-energy *special* boundaries by incorporation of either or both of a step-like structure or misfit dislocations. These special low-energy boundaries often have a periodic structure for specific misorientation angles of the two adjacent grains. The most useful concept for the description of the geometrical relationship in this case is provided by the coincidence site lattice (CSL) model (Bollmann 1970). It will be shown in this paper that this model is applicable to covalently bonded structures with the diamond cubic lattice, and that it is possible to develop structures of specific (coincidence) and some arbitrary (near-coincidence) boundaries. Attention was given to ⟨011⟩ tilt boundaries, largely because a comparison with models of other authors (Hornstra 1959, Kohn 1958) is possible.

---

† *Present address*: *Institut für Metallphysik of the University of Göttingen*, Hospitalstr. 12, 34 Göttingen, F.R. Germany.

0141-8610/81/4304 1045 $02·00 © 1981 Taylor & Francis Ltd

§ 2. [011] CSL ORIENTATIONS

It is convenient for the following to describe the diamond cubic lattice by the tetragonal unit cell given by (fig. 1) : $\mathbf{a}_1 = a[100]$, $\mathbf{a}_2 = a/2[011]$, $\mathbf{a}_3 = a/2[011]$, volume $V_L = a^3/2$. (Planes and directions quoted will all refer to the conventional diamond f.c.c. unit cell—lattice constant a—unless otherwise stated.) When considering grain boundaries between two grains with the diamond cubic structure, rotation of one grain with respect to the other around a common [011] axis can create a superlattice—the CSL—for specific misorientations which contains the lattices of both grains as sublattices. $(01\bar{1})$ is a symmetry plane and the vector $[k_1 k_2 0]_{\mathrm{tetr}}$ therefore becomes coincident with $[k_1 \bar{k}_2 0]_{\mathrm{tetr}}$ of the unrotated lattice after a rotation of $\theta = 2 \arctan k_2/k_1 R$ ($R = \sqrt{2}$) (fig. 1). The CSL established by this rotation angle θ is tetragonal and can be described by the basis vectors $\mathbf{b}_1 = a[k_1 k_2 0]_{\mathrm{tetr}}$; $\mathbf{b}_2 = a[k_2 k_1 R^2 0]_{\mathrm{tetr}}$; $\mathbf{b}_3 = \mathbf{a}_3$ (k_1 and k_2 or k_2 and $k_1 R^2$ have to be divided by common integer factors). The unit cell of the CSL is similar to the unit cell of the direct lattice with the ratios

Fig. 1

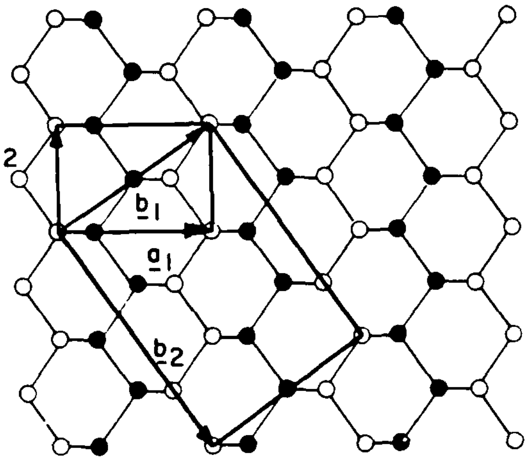

Projection of the diamond cubic lattice on a (011) plane. The filled and open circles are atoms at height 0 and $a\,2\sqrt{2}$ respectively. $\mathbf{a}_1$, $\mathbf{a}_2$ are basis vectors of the direct lattice, $\mathbf{b}_1$, $\mathbf{b}_2$ are basis vectors of the CSL.

$$b_2/b_1 = a_1/a_2 = R.$$

The volume of the CSL unit cell V_c is equal to ΣV_L with $\Sigma = k_1^2 R^2 + k_2^2$ (or $\Sigma = \frac{1}{2}(k_1^2 R^2 + k_2^2)$, if $k_1^2 R^2 + k_2^2$ is even).

The CSL is invariant to a translation of each sublattice by one of its lattice vectors (Bollmann 1970). It is the special property of the [011] rotation axis for the diamond cubic CSL that the number of coincidence sites within the unit cell of the CSL can be increased, in the cases where $k_1^2 R^2 + k_2^2$ is odd, by the translation $\frac{1}{4}a\langle 111\rangle$ of one lattice. If allowance is made for that translation, the ratio of atoms which are in coincidence is given by Σ. (100) is another symmetry plane of the lattice perpendicular to the first. Therefore, the same CSL can also be created by a rotation of $\phi = 180 - \theta$.

For a fixed misorientation of the two lattices, two degrees of freedom remain for the orientation of the boundary plane. Periodic boundary structures occur if the boundary plane is a lattice plane of the CSL. Only symmetric tilt boundaries, where the boundary plane contains the [011] direction and is a mirror plane of the CSL, will be discussed in detail.

§ 3. APPROXIMATE CALCULATION OF THE ENERGY OF A GRAIN BOUNDARY

The wavefunctions forming a covalent bond are well localized and it is likely that only a very limited amount of relaxation in bond length or bond direction is possible. Therefore, a randomly oriented boundary must contain a number of unsaturated bonds. Nevertheless, bond rearrangement may occur and result in distorted bonds; the approximate energy of a boundary is given by

$$E = nE_1 + \sum_i E_2{}^i(\alpha_i), \tag{1}$$

where E_1 is the mean energy of a broken bond, n their number, and $E_2{}^i$ the energy of the ith distorted bond. E_1 is known for a variety of covalent materials (Pauling 1960)—for example, for Si, $E_1 = 1{\cdot}84$ eV, and for Ge, $E_1 = 1{\cdot}64$ eV. $E_2{}^i$ depends on the distortion angle α_i and can be approximated from the elastic constants of the crystal under consideration. In the diamond cubic structure, all bonds are directed along ⟨111⟩ and an elastic shear on a {111} plane results in an angular distortion of those bonds which are aligned perpendicular to this plane. Therefore, at least for small distortion angles α_i, the elastic shear energy per unit volume V is

$$E/V = \tfrac{1}{2}\mu \sin^2 \alpha,$$

where μ is the shear modulus on {111}; E/V can be set equal to the energy of the distorted bonds. There are two bonds perpendicular to the {111} plane per unit cell volume V_L; therefore, we obtain

$$E_2{}^i(\alpha_i) = E_2 \sin^2 \alpha_i. \tag{2}$$

E_2 is equal to $\mu a^3/8$ and may be calculated for Si or Ge; $E_2 = 7{\cdot}2$ and $6{\cdot}6$ eV respectively. Assuming for the time being that eqn. (2) is valid for all distortion angles, a distorted bond has to be considered broken if $E_2{}^i(\alpha_i) = E_1$ which occurs for $\alpha_i \approx 30°$ for both Si and Ge.

The energy $E_2{}^i(\alpha_i)$ is likely to increase faster with angle α_i than predicted by eqn. (2), and the total boundary energy will therefore be underestimated. Additionally, an energy term due to changes of the bond length has been omitted because of the lack of appropriate data. However, the maximum distortion of the bonds across the boundary (i.e. the bonds connecting the two grains) will be lowered if one allows the atoms to relax in the vicinity of the boundary, thus lowering the total energy again. Therefore, it is assumed that eqn. (2) is a fairly good approximation of the boundary energy at 0 K.

Boundaries were formed by simple geometrical fitting of the bonds of the two lattices across the boundary plane and, in general, some relative translation was

Calculated ⟨011⟩ CSL boundary energies γ (in erg/cm^2) for Si (for Ge: multiply by 0·92). $1/\Sigma$ = fraction of coincidence sites for the misorientation angle θ.

Σ	33	19	∞	9	3	17	3	11	9	∞
θ	20·05	26·53	29	38·94	70·53	93·37	109·47	129·52	141·06	150
γ	1740	1170	2550	1310	30†	2380	1760 (2410)‡	1940	1990 (2320)§	2540

† Approximately half of the stacking fault energy of Si.
‡ Energy of the ($\Sigma = 3$) lateral twin boundary proposed by Hornstra (1959).
§ Energy of the non-faceted ($\Sigma = 9$) boundary.

necessary to minimize the energy of the distorted bonds. A few random boundaries with a common ⟨011⟩ axis were also constructed in this way, but their energy was very insensitive to such translation ($\theta = 29°$ and $150°$, the table). An average energy per unit area γ was obtained whose values, ~ 2500 erg/cm^2 for Si and ~ 2300 erg/cm^2 for Ge, are lower than twice the surface energy of a comparable† {110} surface of these materials (Jaccodine 1963), 3020 erg/cm^2 for Si and 2600 erg/cm^2 for Ge. Thus, a binding force exists between the two grains.

The energy for CSL boundaries was in general lowest if the boundary was parallel to a $(100)_{\mathrm{CSL}}$ plane, the boundary with the shortest periodicity for a given Σ. Occasionally, however, other planes like $(010)_{\mathrm{CSL}}$ or $(110)_{\mathrm{CSL}}$ (or even higher index planes) had to be considered. CSLs up to $\Sigma = 33$ yielded boundaries with energies lower than the average value of a random one. All calculated values are listed in the table and shall now be discussed in detail.

§ 4. Models of CSL low energy boundaries

The boundaries of low energy have common features and can be divided into two groups.

(*a*) Rotation angles $0° < \theta \leqslant 70{\cdot}53°$. The few special boundaries found in this range have $\Sigma = 1 + 2n^2$ ($n = 1, 2, 3, 4$) and contained only distorted bonds (figs. 2–5). With the exception of the $\Sigma = 3$ boundary, all boundaries can be considered as an array of the same type of defect—a five- and a seven-membered ring of atoms—at different spacings.

Fig. 2

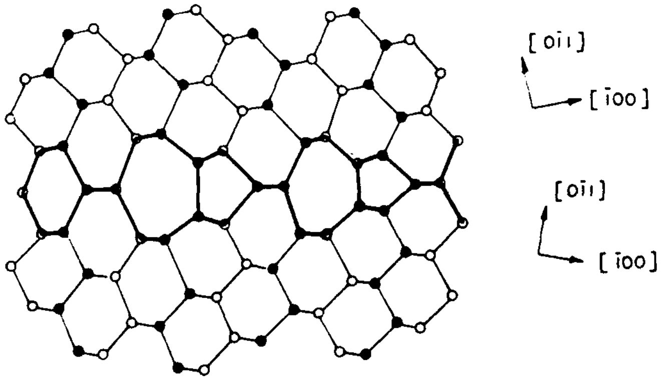

[011] projection of the ($\Sigma = 33$) symmetric tilt boundary, $\theta = 20{\cdot}05°$.

---

† The random boundaries had on average 3 bonds/a^2, comparable to 2·8 bonds/a^2 for a {110} surface.

Fig. 3

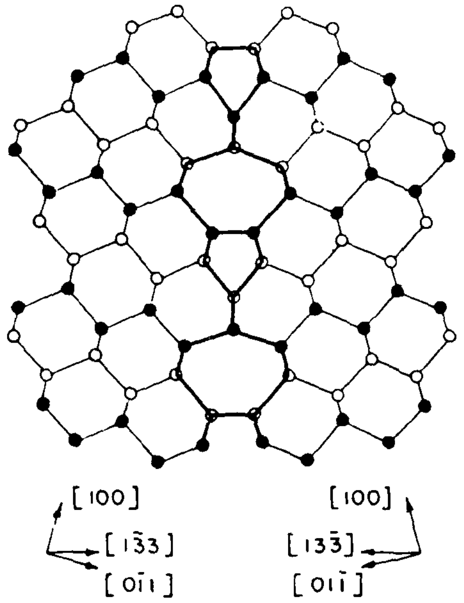
[100]
$[1\bar{3}3]$
$[0\bar{1}1]$
[100]
$[13\bar{3}]$
$[01\bar{1}]$

[011] projection of the ($\Sigma=19$) symmetric tilt boundary, $\theta=26\cdot53°$.

Fig. 4

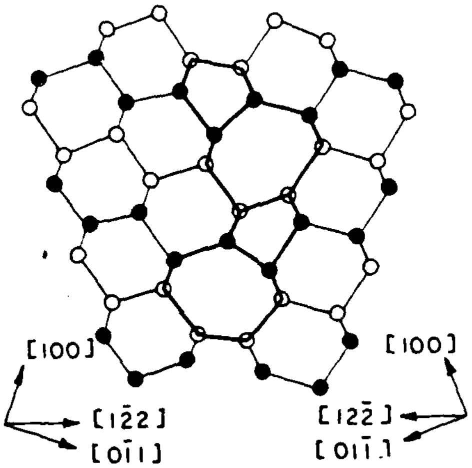
[100]
$[1\bar{2}2]$
$[0\bar{1}1]$
[100]
$[12\bar{2}]$
$[01\bar{1}]$

[011] projection of the ($\Sigma=9$) symmetric tilt boundary, $\theta=38\cdot94°$ (second-order twin boundary).

Fig. 5

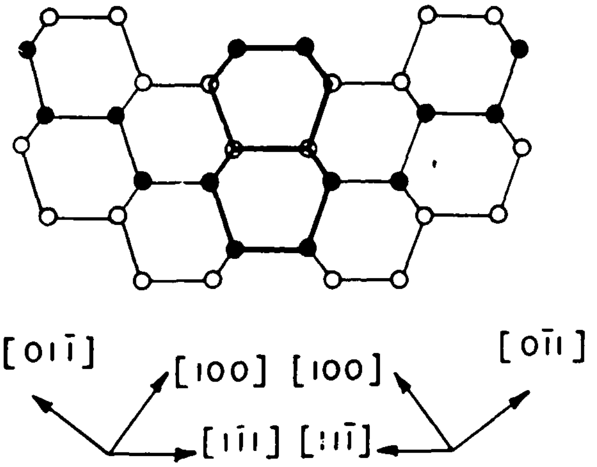

[011] projection of the ($\Sigma=3$) symmetric twin boundary, $\theta=70{\cdot}53°$.

The structures shown here for the $\Sigma=19$ and 9 boundaries have been proposed earlier (Hornstra 1959). He constructed a number of high-angle tilt boundaries in the diamond cubic structure as arrays of edge dislocations and pointed out that these five- and seven-membered ring defects are edge dislocations, with a Burgers vector $\mathbf{b}=a/2[01\bar{1}]$ and a (100) glide plane. It is tempting to suggest that for all misorientations of the two grains $\theta\leqslant 26{\cdot}53°$ ($\Sigma=19$), the boundary can be considered a small-angle tilt boundary consisting of these edge dislocations. This view is supported by the observation (Bourret and Desseaux 1979) that this type of edge dislocation could be identified in small-angle boundaries with $\theta\approx 5°$ by lattice imaging.

The energy per unit area of a small-angle boundary has been calculated (Hirth and Lothe 1968 a) for the whole range of misorientations, and can be given by

$$\gamma=\gamma_0\theta\left\{\frac{\theta}{2\theta_{\mathrm{m}}}\coth\frac{\theta}{2\theta_{\mathrm{m}}}-\ln\left(2\sinh\frac{\theta}{2\theta_{\mathrm{m}}}\right)\right\}, \tag{3}$$

where $\gamma_0=\mu b/4\pi(1-\nu)$ and $\theta_{\mathrm{m}}=b/2\pi r$. (Here r is the core cut-off radius of the edge dislocation.) This equation has been fitted to the calculated boundary energies of $\Sigma=33$ and 19 (fig. 6) and yielded values for the parameters $\gamma_0=17\,300\ \mathrm{erg/cm^2}$ and $r=1{\cdot}16b$. The first value does not agree with the calculated γ_0 of $\sim 2000\ \mathrm{erg/cm^2}$, but the cut-off radius is only somewhat higher than expected for an edge dislocation in the diamond cubic lattice, for which $r\approx 0{\cdot}3b$ was proposed (Hirth and Lothe 1968 b). Equation (3) is not valid if the cores of the dislocations overlap, which occurs for $\theta>26{\cdot}53°$. Consequently, those boundaries cannot be considered small-angle boundaries, although the edge dislocation structure still can be distinguished in the $\Sigma=9$ boundary. Thus it

Fig. 6

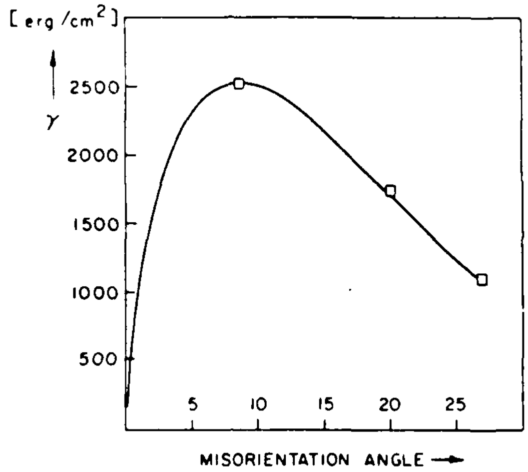

Energy (per unit area) γ of a small angle tilt boundary versus misorientation angle θ (eqn. (3)). The squares are the calculated CSL grain boundary energies. See text for further discussion.

is unlikely that the energy of boundaries with $\theta > 26{\cdot}53°$ can be calculated from the energy of their individual edge dislocations. The high energy of the random boundary ($\theta = 29°$, the table) indeed shows that eqn. (3) is not valid for $\theta > 26{\cdot}53°$.

The first- ($\Sigma = 3$) and second-order ($\Sigma = 9$) twin boundaries with $(100)_{\mathrm{CSL}}$ plane have been thoroughly investigated previously (Hornstra 1959, Kohn 1958). The models given in these papers agree with those given here ; the $\Sigma = 9$ boundary has been confirmed by lattice imaging (Krivanek *et al.* 1977). It should be mentioned that in all cases studied so far, relative displacement of the two grains parallel to the boundary plane was unnecessary to achieve a minimum bond distortion.

(*b*) Rotation angles $70{\cdot}53° < \theta \leqslant 180°$. The four special boundaries found in this range each contained unsaturated bonds (figs. 7–10). The $\Sigma = 3$ and 9 boundaries are identical to the corresponding CSL boundaries with a rotation angle of $(180 - °\theta)$ and a $(010)_{\mathrm{CSL}}$ boundary plane. Hornstra (1959) and Kohn (1958) propose slightly different structures for $\Sigma = 3$, but their models also contain the same number of broken bonds, if one considers that Kohn's atoms with five or three neighbours are equivalent to one unsaturated bond. Hornstra's model has more distorted bonds resulting in a higher energy (the table) ; we therefore believe our structure, which is essentially the same as Kohn's, is more likely. In his investigation of twin boundaries, Kohn pointed out that in some cases one can achieve a better geometrical fitting by faceting the boundary, thus increasing the number of coincidence sites in the boundary. Indeed, the faceted structure proposed for the $\Sigma = 9$ lateral boundary has a lower energy than the unfaceted boundary plane (see the table).

Fig. 7

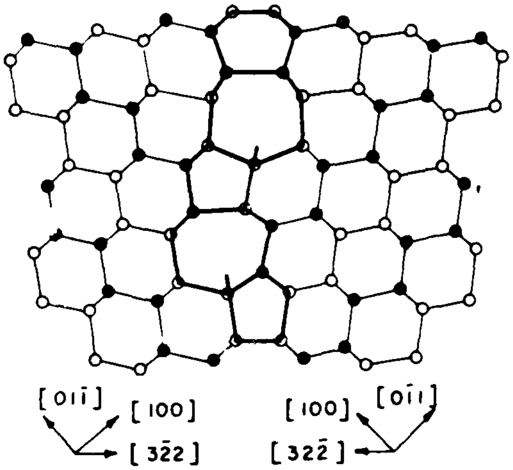
$[01\bar{1}]$
$[100]$
$[3\bar{2}2]$
$[100]$
$[0\bar{1}1]$
$[32\bar{2}]$

[011] projection of the ($\Sigma = 17$) symmetric tilt boundary, $\theta = 93{\cdot}37°$.

The structure for $\Sigma = 11$ differs again from Hornstra's model. He assumes a relative translation of the two grains along their common [011] axis by $a/4\sqrt{2}$, which, however, introduces more distorted bonds. The number of unsaturated bonds remains the same as in the structure proposed here. The CSL model leads additionally to a $\Sigma = 17$ and a $\Sigma = 27$ boundary ; the energy of the former

Fig. 8

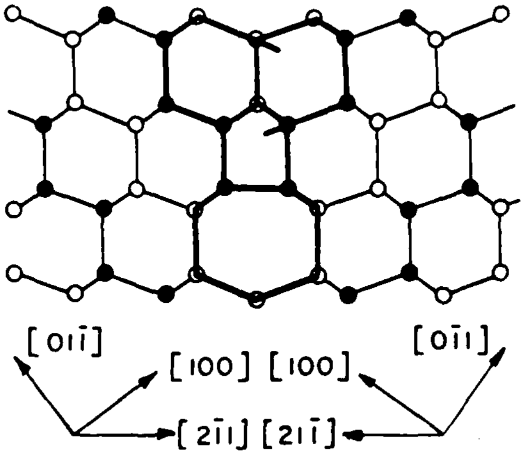
$[01\bar{1}]$
$[100]$
$[100]$
$[0\bar{1}1]$
$[2\bar{1}1]$
$[21\bar{1}]$

[011] projection of the ($\Sigma = 3$) lateral twin boundary, $\theta = 109{\cdot}47°$.

Fig. 9

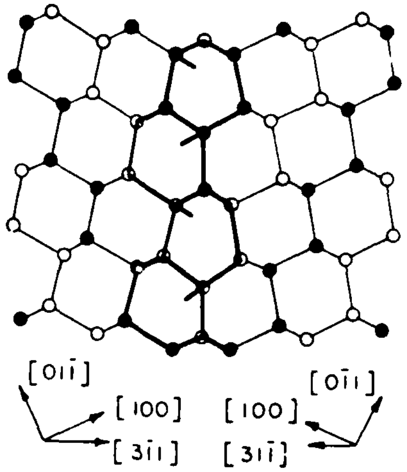

[011] projection of the ($\Sigma = 11$) symmetric tilt boundary, $\theta = 129{\cdot}52°$.

Fig. 10

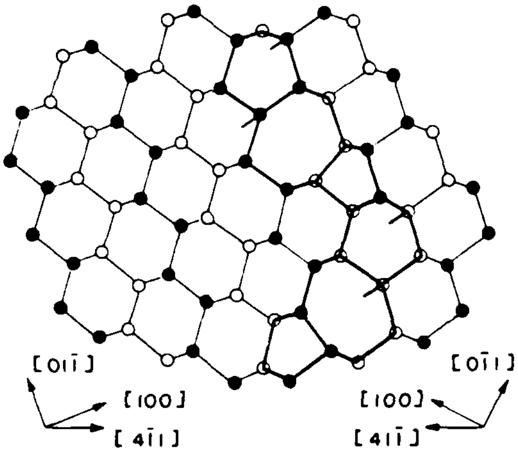

[011] projection of the ($\Sigma = 9$) symmetric tilt boundary, $\theta = 141{\cdot}06°$ (second-order lateral twin boundary).

boundary is slightly lower than the energy of random boundaries. Other CSL tilt boundary planes than those presented here all have structures and energies which are indistinguishable from random boundaries.

§ 5. CONCLUSION

The application of the CSL model to the diamond cubic lattice allows a systematic determination of low energy 'special' boundaries. An array of five- and seven-membered rings of atoms (with or without a broken bond) is the common feature of all boundaries. The essential similarity of the proposed structures with those of other authors who approached the problem differently shows that the ambiguity involved in a purely geometric modelling is not serious for this structure. Apart from the well established first- and second-order twin boundaries, boundaries with $\Sigma = 11$ and 19 should exist. Boundaries within the range $\theta \leqslant 26{\cdot}53°$ ($\Sigma = 19$) can be considered as small angle boundaries, the five- and seven-membered rings without broken bonds being edge dislocations in the diamond cubic structure.

The application of this method to near-coincidence orientations involving misfit dislocations and to inclined boundaries is possible and shall be discussed in a forthcoming paper. The extension of this approach to materials crystallizing in the structurally-related zinc blende and wurtzite structures is evident.

ACKNOWLEDGMENTS

This work was supported by Battelle Columbus Laboratories and the Air Force Office of Scientific Research under Contract No. F49670-78C-0053. The author wishes to thank Professor A. H. Heuer for his kind hospitality, encouragement and for many useful discussions.

REFERENCES

BOLLMAN, W., 1970, *Crystal Defects and Crystalline Interfaces* (Berlin: Springer-Verlag).

BOURRET, A., and DESSEAUX, J., 1979, *J. Phys., Paris*, **40,** C6, 7.

HIRTH, J. P., and LOTHE, J., 1968 a, *Theory of Dislocations* (New York: McGraw-Hill Book Company), p. 672; 1968 b, *Ibid.*, p. 211.

HOLT, D. B., 1964, *J. Phys. Chem. Solids*, **25,** 1385.

HORNSTRA, J., 1959, *Physica*, **25,** 409; 1960, *Ibid.*, **26,** 198.

JACCODINE, R. J., 1963, *J. electrochem. Soc.*, **110,** 524.

KOHN, J. A., 1958, *Am. Mineral.*, **43,** 263.

KRIVANEK, O. L., ISODA, S., and KOBAYASHI, K., 1977, *Phil. Mag.*, **36,** 931.

PAULING, W., 1960, *The Nature of the Chemical Bond* (Cornell University Press), p. 85.

Appendix 4

ON THE EFFECTS OF DIHEDRAL ANGLE AND PRESSURE ON THE DRIVING FORCES FOR PORE GROWTH OR SHRINKAGE

R. M. Cannon

INTRODUCTION

At high temperatures, pores in polycrystalline materials can either shrink or grow as a result of diffusional transport of atoms to or from the pores. In principle, two separate processes can be considered. In one case mass is exchanged between pores and grain boundaries (or dislocations) which leads to changes in the apparent density and bulk dimensions of the polycrystal. In the other, mass can be exchanged between pores which leads to a change in the size distribution of the pores but not in the total pore volume or external dimensions of the polycrystal. The problems of pore coarsening and densification or cavity growth have been treated extensively, although the problems are usually treated separately. From these separate treatments it is easily seen that applied stresses should affect densification more than coarsening, and that the occurrence of one of these processes should affect the driving force for the other. However, some more specific coupling between the various processes are seen when they are considered together.

It is generally recognized that the driving force for density changes depends both on applied stresses and on surface tension forces whereas the driving force for pore coarsening results from differences in surface tension forces at pores of different sizes. For isotropic materials attention is usually focused on the pore curvature when considering these driving forces, although it is recognized that forces due to surface tensions can also be important. Because the dominant terms are usually a result of surface curvature, it is clear that for materials with high grain boundary energies and low dihedral angles the surface curvatures and driving forces for densification will be affected. The initial modeling which was based only on curvature considerations suggested that low dihedral angles would reduce the driving force for densification, that pores with many sides (i.e., many neighboring grains) would have a lower driving force for densification, and that pores with many sides and low dihedral angles may grow instead of shrink.

However, the problem is incomplete as modeled because the site for mass exchange with the pore was not considered.

In the present paper we reconsider the driving forces for pore growth or shrinkage using a simple two dimensional model. The results indicate the average driving forces for pore growth or shrinkage and the existence of some equilibrium conditions. The inclusion of the surface tension forces allows a more specific statement of the effect of low dihedral angles on densification. In addition, some interesting cases of coupling between densification and pore or grain growth are elaborated.

THEORY

1. Basic Considerations

For a porous polycrystal at low stresses, pore growth or shrinkage can result from defect diffusion between pores and sites of lattice discontinuity such as grain boundaries or dislocations. Within good lattice the driving force for diffusion is proportional to $\nabla(\mu-\mu_v)$ where μ is the chemical potential for atoms, and μ_v is that for vacancies. If surfaces and boundaries act as efficient sources and sinks for point defects then they will come to local equilibrium and provide boundary conditions for the distribution of $(\mu-\mu_v)$. The commonly presumed conditions are that at planar grain boundaries,

$$\mu - \mu_v = \mu = \mu_o - \sigma_{nn}\Omega \quad , \qquad (1\text{-a})$$

that across curved grain boundaries,

$$\Delta(\mu - \mu_v) = \Delta\mu = \kappa\gamma_b\Omega \quad , \qquad (1\text{-b})$$

and that at free surfaces,

$$\mu - \mu_v = \mu = \mu_o - \sigma_{nn}\Omega + \kappa\gamma_s\Omega \quad , \qquad (1\text{-c})$$

where σ_{nn} is the normal stress acting at an interface, Ω is the atomic volume, κ is the curvature, γ_b is the grain boundary tension, and γ_s is the surface tension. In addition, in many cases there may be rapid diffusion along boundaries and surfaces in response to $\nabla\mu$ as give by Eqs. (1) assuming point defect equilibration is rapid compared to diffusion.

At equilibrium $\mu_v = 0$ and μ will be uniform throughout for a single component system. However, equilibrium does not obtain for many problems of interest, and to treat the nonequilibrium, kinetic problems it is desirable to know the distribution of $\mu-\mu_v$. It can easily be appreciated that in nonequilibrium situations the distribution of $\mu-\mu_v$ and of the stresses inside grains will depend on the dominant transport mechanisms, as these will affect the local stresses and interface curvatures. For a multicomponent system the situation becomes more complex but analogous. These problems are difficult to solve in general, particularly when considering the possibility of non-hydrostatic stresses or arrays of pores of different sizes. Thus it is useful to simplify the treatment in order to obtain average potentials at specific segments of interfaces. The result of such a treatment gives metastable equilibrium conditions where they exist and an indication of the directions for and average driving forces for densification and pore growth processes.

When considering the microstructural evolution of a porous polycrystal there are three processes of interest to be considered in the simplest situations. These are: (1) density changes which occur by transport of atoms between grain boundaries and pores (assuming there are no dislocations); (2) pore coarsening which involves transport of mass between pores; and (3) grain growth which results from the disappearance of small grains and the growth of large grains as grain boundaries migrate toward their centers of curvature. In addition, in inhomogeneous materials, processes of grain shape change and grain boundary sliding will also occur. Some interesting aspects regarding these processes can be easily seen from a model of a two dimensional array of pores and grains. Several interesting results are obtained which are expected to be general for three dimensions. In addition, there are some results which are artifacts of the simple model, but which are nonetheless curiously interesting.

2. Thermodynamic Potentials

For a complete treatment of the range of problems of interest, it is desirable to determine the potential $\mu-\mu_v$ throughout all regions of perfect lattice and the potential μ at all interfaces and dislocations for conditions of non-hydrostatic applied stresses and non-uniform internal stresses. The chemical potentials can be found as derivatives of an appropriately chosen free energy. The Gibbs free energy as usually expressed,

$$G = F + pV \, , \tag{2}$$

where F is the Helmholtz free energy, p the pressure and V the system volume, is inappropriate or inconvenient for several reasons, but can be suitably redefined to be useful for the present problem. If the stresses are non-hydrostatic, the pV term does not adequately describe the change in the external work potential which may arise from additions of mass or changes of volume of the material. This has been discussed by Gibbs and extensively since. The reason can be readily appreciated by realizing that additions of mass in different ways which would result in different shapes of the body or different surface displacements would cause different amounts of external work. Further, even in the limiting case where an external hydrostatic stress is applied, the bulk volume is not a state function for a porous material and so is an inconvenient variable.

For the present purposes it is convenient to define the system as the aggregate of condensed phases, and it is sufficient to generalize to the case where the tractions are not the same at all surfaces, but where along any particular surface there is only a normal traction, i.e., the local stresses at the surface are

$$\sigma_{nn} = -p \tag{3a}$$

and

$$\sigma_{nt} = \sigma_{nt'} = 0 \, , \tag{3b}$$

where n is the normal coordinate axis and t and t' are tangential to the surface. If there are a finite number of regions along the surface where the pressure is uniform, i.e. p_i, then a useful free energy is

$$G' = F + \sum p_i \Delta V_i' = \int \frac{\overline{F} dV}{\Omega} + \sum p_i \Delta V_i' \, , \tag{4}$$

where $\overline{F}$ is the Helmholtz free energy per atom for the local composition and elastic stresses, (σ_{ij}), and Ω is the atomic volume. The change in the work potential of the exterior can be considered as a series of reservoirs at different pressures. The total volume of condensed phases in the piece (i.e. the system volume) is

$$V = \sum \Delta V_i' \ , \tag{5}$$

where each $\Delta V_i'$ represents the volume change of a particular reservoir due to the system; these may be expressed as

$$\Delta V_i' = V_{oi}' - V_i' \ , \tag{6}$$

where V_{oi}' is the reference volume for the ith reservoir and V_i' is the current volume for the ith reservoir.

The chemical potential for any species can be defined in the usual way as

$$\mu_k = \left.\frac{\delta G'}{\delta n_k}\right|_{T,p_i,n_\ell} \ . \tag{7}$$

The procedure is useful for atoms or defects. For either it may be anticipated that within good lattice unique values of the individual potentials may not exist. However, for physically interesting problems the important quantities are the differences in chemical potentials between substitutional species, and these will be unique. That is, only exchanges of species which preserve the lattice are meaningful unless new lattice sites are created. The free energy changes for these operations are differences in potentials between the species, and these are unique quantities. New lattice sites can only be created at sites of lattice discontinuity, and at these sites the potentials of the individual species will be unique. For the present we will assume that the boundaries and surfaces are incoherent and good sources or sinks for point defects and so, at the interfaces, all species are at local equilibrium. (Dislocations will be assumed to be absent.)

The first term in Eq. (4) includes the elastic strain energies and so the chemical potentials include terms of order $\sigma^2\Omega/2E$. For most sintering and coarsening problems these terms are small and will be ignored. The dependence of F on composition is not generally negligible, and must be considered to explicitly treat segregation which may result for either thermodynamic or kinetic reasons. Presently, we confine our considerations to single component materials or stoichiometric compounds.(*) Finally, F contains surface energy terms of the form $\int \gamma_j dA_j$ for each type of interface. If the material is sufficiently free of surface active impurities that no depletion or enrichment of surfaces occurs, and if the interfaces are isotropic, then all $\delta\gamma_j = 0$.

Thus, the free energy in Eq. (4) reduces to that for a single component, isotropic, rigid lattice system of n atoms (or "molecules"). If only constant pressure conditions are considered, then it is convenient to use

$$G = G' - \sum p_i V'_{oi} \,, \tag{8}$$

so that G contains only terms which are variable, i.e.,

$$G = nF_o - \sum p_i V'_i + \gamma_b A_b + \gamma_s A_s \,, \tag{9}$$

where A_b and A_s are the grain boundary and surface areas, respectively.

The chemical potential for atoms at a particular location can be determined as:

$$\mu_k = \left.\frac{\delta G}{\delta n}\right|_{T,p_i} = \mu_o - \sum p_i\left(\frac{\delta V_i}{\delta n}\right) + \gamma_b\left(\frac{\delta A_b}{\delta n}\right) + \gamma_s\left(\frac{\delta A_s}{\delta n}\right) \,, \tag{10}$$

where $\mu_o = F_o$. Clearly, for a single component system the chemical potential will depend on the extent to which work is done against a particular reservoir and a particular interfacial area is changed. In general, it will be

---

(*)For a compound with a narrow range of stoichiometry, under nonequilibrium conditions slight non-stoichiometry will develop primarily near the interfaces due to the differences in the diffusivities. This will adjust the potentials to cause stoichiometric transport. For our purposes, compounds can be considered single component if all transfers are taken to involve stoichiometric quantities.

different throughout the system. If the surface tension terms are small, the only condition for equilibrium is if all the p_i are equal. If not, the body will have non-hydrostatic elastic stresses. These can be maintained in mechanical equilibrium, but cause a chemical potential gradient which is a driving force for diffusion which would lead to a continuous shape change. If the pressure is not the same on all surfaces, the only way in which equilibrium can be obtained, i.e., μ the same everywhere, is if the surface tension terms become large.

For the present paper, the chemical potentials at different locations in polycrystalline arrays will be considered. Attention will be confined to the potentials at boundaries and surfaces. When these are equal on all surfaces, then no diffusion potentials will exist, the point defect concentrations in the grain interiors will become uniform and at $\mu_v = 0$, and the values of μ in the interior will be clearly defined.

3. Geometrical Arrays

To evaluate the driving forces it is desirable to consider a model in which both the size and the number of sides of pores or grains can be considered as separate variables. We consider a nearly infinite two dimensional network of pores and grains. The network can be considered to be externally loaded in various ways. Here we consider only the case where it is immersed in a hydrostatic reservoir at pressure p_e. To simulate the situation of open, interconnected porosity, the pressure in all pores would be equal to p_e. For the more interesting case of closed porosity, the pressures in different pores can be different from p_e and from each other and taken as p_{pi} for the ith pore. For this situation the free energy expression in Eq. (10) becomes:

$$G = nF_o - \sum p_{pi}V_{pi} - p_eV_e + \gamma_bA_b + \gamma_sA_s \ . \qquad (11)$$

To maintain correspondences with the three dimensional problem we can consider a unit depth of material and refer to three dimensional quantities such as volumes and pressures. Although the two dimensional problem is simpler than the three dimensional one, a general treatment of an arbitrary array of pores and grains is still formidable. A range of more simplified arrays can be analyzed which give insight into the problems associated with sintering.

Arrays which are periodic can be analyzed simply, and can be conceived as part of an infinitely large array of grains and pores. The simplest arrays can be made somewhat artificial by keeping some variables uniform. This feature leads to a few interesting but perhaps unrealistic results. It has the advantage that the effects of different variables or free energy terms can be considered separately. With appropriate interpretation most of the results anticipated for realistic arrays can be seen and the expected results for three dimensional arrays approximated.

Several periodic and repeatable arrays which fill two dimensional space can be made from circles of the same size, but which result in pores with different sizes or numbers of sides. With reference to the sintering problem it is easy to conceive of these arrays as resulting from the packing of circles (or rods) in the specified arrangements and sintering beyond the initial stage. Qualitatively, there are several different types of arrays which differ in the degree to which the local geometry can be easily characterized or specified. There are three arrays in which the grains are identical and all of the pores are identical and for which the grains and pores are symmetrical. These can be obtained from hexagonal packing of circles, square packing of circles, and hexagonal packing of circles with 1/3 of the circles missing, Figure 1. These are characterized as 3-(6+3), 4-(4+4), and 6-(3+3), respectively, where the first number is the number of sides per pore and the number of sides per grain is given in parentheses as the sum of the number of grain boundaries and pore faces. The second class of arrays considered here are those in which n' circles are packed in repeatable cells of n'+1 sites, Fig. 2. These give a combination of one six-sided pore and several three-sided pores per cell. These arrays are also amenable to considerable analysis because both types of pores are symmetrical and the geometry can be plausibly specified and characterized. Arrays in which the pores are asymmetric or have more than one type of facet are of interest, but can only be treated more approximately. These include arrays of 5-sided pores with equal numbers of 7-sided grains and packing accidents involving clusters of missing particles, i.e. divacancies, trivacancies, etc., up to large holes.

4. Triple Point Equilibria

For two dimensional networks, only junctions between three interfaces are stable. Although junctions of four or perhaps more interfaces would form occasionally under non-equilibrium conditions, they are sufficiently unstable that they would decompose rapidly. Thus, we only consider networks with three interface intersections. The exception to this which is of some interest occurs when large pores disappear which would lead to an instability.

At three interface junctions, local force balance or energy minimization dictates that the interfaces meet at the equilibrium dihedral angles. For three grain boundary junctions, this requires 120° angles between grain boundaries. For grain boundary-pore intersections, the equilibrium angle depends on the ratio of γ_b/γ_s as

$$\cos(\phi/2) = \gamma_b/2\gamma_s \ . \tag{12}$$

(The angle ϕ is defined in Fig. 3.)

5. Pore Geometry

Under non-equilibrium conditions, the chemical potentials will vary continuously along all interfaces (assuming they are good point defect sources), and the chemical potentials must be continuous at triple points. Thus, from Eqs. (1c) and (1a) it can be seen that the radius of curvature of the pores will vary continuously as will the normal stresses acting on boundaries. The actual pore shapes and stress distributions along boundaries will depend on the dominant transport mechanism. However, at triple points very little atomic transport is needed to establish the equilibrium dihedral angle. Thus, it is both energetically favorable and kinetically possible that the equilibrium dihedral angles will establish quickly even at the expense of inducing higher curvature in adjoining segments of some interfaces.

At equilibrium, uniformity of the chemical potential along the pore surfaces requires that each pore segment be a circular arc. Similarly, the stresses along the boundary must be uniform. These conditions follow directly from calculations of the requirements for complete equilibrium. To obtain approximate driving forces for transport in non-equilibrium conditions requires rigorous kinetic calculations or some simplifications. To do the latter here we assume that the pores are bounded by segments of circles which meet at the equilibrium dihedral angle at the grain junctions. With those assumptions, average chemical potentials can be calculated for pore surfaces or grain boundary segments from Eq. (11). Although the normal grain boundary stresses need not be calculated explicitly, only average potentials are obtained which are equivalent to those which would result assuming the boundary segment were uniformly stressed.

For symmetrical, equilibrium pores, the sign and magnitude of the radius of curvature can be explicitly determined and will depend on the pore area, the dihedral angle, and the number of sides of the pore, N. The pertinent geometrical terms are defined in Figure 3. The chemical potentials are most conveniently described in terms of the radius of curvature, R. For large dihedral angles the pore surfaces will be concave and we take $R < 0$ for this situation. For small dihedral angles the pore surfaces will be convex, for which $R > 0$. Obviously, for some dihedral angle, ϕ_c, the pores will have straight sides, i.e. $R \to \infty$. This critical angle will be larger for pores with many sides, i.e.,

$$\phi_c = \pi(1 - 2/N) \ . \tag{13}$$

For a given N, the dependence of R on pore size and ϕ can be seen from:

$$R = \frac{-S}{2 \sin \Delta\phi/2} \ , \tag{14}$$

where $\Delta\phi = \phi - \phi_c$. The size of the pore is more conveniently visualized in terms of r, the radius of the circle which circumscribes the pore. However, the relationships between R and the pore area A, or r, are more cumbersome. We note that as N increases or ϕ decreases the ratio r/R increases algebraically (note that $-1 \leq r/R$) and that the ratio $A/\pi r^2$ decreases as N or ϕ decrease.

As will become apparent, in some cases it is useful to describe the results either in terms of the fractional porosity or in terms of the initial configuration of circles used to construct the arrays. For the arrays considered which are made up initially of n' or (n'+1) circles of diameter D_o on (n'+1) sites the porosity, v_f, can be expressed as

$$v_f = \sum \frac{n_{ci}}{(n'+1)} \left(\frac{r_i}{D}\right)^2 f_i(\phi) \ , \tag{15a}$$

or, unless $R = \infty$, as

$$v_f = \sum \frac{n_{ci}}{(n'+1)} \left(\frac{R_i}{D}\right)^2 g_i(\phi) \ , \tag{15b}$$

where there are n_{ci} pores of a particular type (i.e. N) and size in the cell; the geometrical factors depend on N and the packing configuration. The grain size, D, is conveniently defined in terms of the diameter of the sphere that could occupy the site, Figure 4. This is related to D_o by

$$D = D_o \left(\frac{1 - v_f}{1 - v_{fo}}\right)^{\frac{1}{2}} \ , \tag{16}$$

where v_{fo} is the porosity of the initial array which is the maximum possible for that particular packing configuration. Also note that A_o, the initial pore area, depends strongly on N and is the maximum possible for a pore of N sides.

RESULTS

Average driving forces for different processes can be determined by considering the variation in G as given in Eq. (11) for various situations or arrays. From Eq. (11) at constant p_i and p_e ,

$$\delta G = F\delta n - \sum p_{pi}\delta V_i - p_e \delta V_e + \gamma_b \delta A_b + \gamma_s \delta A_s \ . \tag{17}$$

By determining δG subject to appropriate constraints, chemical potentials or chemical potential differences between two locations can be determined. It is useful to first consider mass additions to the polycrystalline arrays in order to indicate the origin of specific driving forces. Then mass exchanges between locations will be considered which represent densification, pore growth, or coarsening processes of interest. In several cases equilibrium conditions are obtained for some processes, but for most cases these are only metastable or quasi-equilibrium conditions.

1. Simple Mass Additions

First consider an addition of mass from an external source to a particular pore surface. For this process

$$\delta n = -\delta V_{pi}/\Omega \ , \tag{18}$$

and for this process all other pores and the external reservoir are left unaffected, i.e.,

$$\delta V_{pj} = \delta V_e = 0 \ . \tag{19}$$

For all of the configurations considered, it can be shown that, if the dihedral angle is the equilibrium value given by Eq. (12), then

$$\gamma_b \frac{\delta A_b}{\delta n} + \gamma_s \frac{\delta A_s}{\delta n} = \frac{\gamma_s \Omega}{R_i} \ , \tag{20}$$

and from Eqs. (17-20),

$$\mu_p - \mu_o = \frac{\gamma_s \Omega}{R_i} + p_{pi}\Omega \ . \tag{21}$$

As can be seen in Figure 3, regardless of the sign or value of R, it is true that $\delta A_b/\delta n > 0$, $\delta A_s/\delta n < 0$, and $\delta|R|/\delta n < 0$. Thus, at $p_{pi} = 0$ the magnitude of $\mu_p - \mu_o$ will increase as ϕ is different than ϕ_c, and will be greater for smaller pores; however, the sign of $\mu_p - \mu_o$ will depend on whether ϕ is large or small relative to ϕ_c. It is worth emphasizing that addition of mass to a particular pore does not result in changes in the conditions elsewhere. Thus even if large additions, Δn, are made to the pore, μ_p depends only on R and p_p for the particular pore.

Alternatively, consider an addition of mass to the grain boundary region. In the rigid lattice approximation even infinitesimal amounts of mass cannot be added to a local region of grain boundary or even around an entire grain because prohibitively high stresses would be developed. There are two alternative ways to proceed. One is to consider the additions spread along the boundaries in such a way that no incompatibilities develop. The simplest way is to consider a uniform addition to all boundaries as shown in Figure 4. The effect of the addition on the pore surface or volume is somewhat arbitrary. If it is prescribed that the addition occurs such that

$$\delta V_{pi} = 0 \ , \tag{22}$$

then

$$\delta A_{si} = 0 \;, \tag{23}$$

and

$$\delta n = -\delta V_e/\Omega \;. \tag{24}$$

Further, for the arrays considered it can be shown that

$$\gamma_b \frac{\delta A_b}{\delta n} = \frac{\gamma_b \Omega}{D} \;, \tag{25}$$

and, from Eqs. (17) and (22-25),

$$\mu_b - \mu_o = \frac{\gamma_b \Omega}{D} + p_e \Omega \;. \tag{26}$$

The second term is expected. The first term has generally not been considered, but the schematic in Figure 4b clearly indicates that if mass is added to the system such that $\delta V_e < 0$ and the number of grains in the array is constant then $\delta A_b > 0$.

Alternatively, a sufficiently small layer of mass may be added locally to a grain boundary region if it can be accommodated elastically. The change in external volume will be that given in Eq. (24) which would lead to the second term in Eq. (26) for μ_b-μ_o. The correspondence with the first term in Eq. (26) is harder to establish. If the added mass is considered as an interstitial dislocation loop along a region of boundary, then there are two terms which could be identified with an increase in A_b. Depending upon where in the net the loop terminates, the edge may be associated with an increase in A_b which formally leads to a term involving $\gamma_b \delta A_b$. In addition, other boundaries in the network will be stretched elastically as part of the elastic accommodation of the loop. However, the work done to stretch the interface elastically is not generally the same as γ_b, which results from increasing A_b by adding more atomic sites and leaving the surface structure statistically unchanged. Further analysis to establish the conditions under which this process gives the potential in Eq. (26) is beyond the present scope, but we make several observations. The local additions of mass will lead to significant stress redistribution if δn becomes appreciable which, of course, must be properly treated in transient processes. In many cases this redistribution is slow enough that Eq. (1a) will still describe $\mu_b-\mu_o$ in terms of the local stresses However, if the minimum admissible δn is sufficiently large that the stresses would be appreciably affected, then neither $p_e\Omega$ nor $\sigma_{nn}\Omega$ may adequately describe the external work and significant changes in the $\int\sigma^2 dV/2E$. This would seem most likely to be a problem in describing problems of relaxation of high local stress concentrations or pore nucleation. Most of the sintering and coarsening problems of interest are quasi-steady problems in which the expression for $\mu_b-\mu_o$ in Eq. (26) gives a correct view if the volume over which mass is spread is properly considered. In these cases the additional mass clearly leads to an increase in the number of grain boundary sites of excess free energy γ_b.

2. Densification

Densification results from transfer of mass from grain boundaries to pore surfaces and results in a change in the external dimensions. The potential difference between the pores and grain boundaries can be determined from

$$\mu_p - \mu_b = \frac{\delta G}{\delta n_p} - \frac{\delta G}{\delta n_b} \quad . \tag{27}$$

This is subject to the constraint that the system volume does not change, $\delta V = 0$, which leads to

$$\sum \delta V_{pi} = -\delta V_e \quad . \tag{28}$$

If exchange between all the boundaries in a cell and all the pores of one particular type in the cell is considered, then

$$\delta n_{pi} = -\delta V_{pi}/\Omega = -\delta n_b = \delta V_b/\Omega \quad , \tag{29}$$

and from Eqs. (17), (27) and (29),

$$\mu_{pi} - \mu_b = -\left[\frac{\gamma_b}{D} - \frac{\gamma_s}{R_i} + p_e - p_{pi}\right]\Omega \quad . \tag{30}$$

A set of relations like Eq. (30) exists for each type of pore. Obviously, $\mu_{pi}-\mu_b$ can be positive, negative or zero, which describes the tendency of the pore to grow, shrink, or be at equilibrium with respect to the grain boundary.

It is possible for a particular pore or set of pores to be at equilibrium with respect to the grain boundaries, i.e. $\mu_{pi} = \mu_b$, when the bracketed term in Eq. (30) vanishes. Several specific situations are worth noting.

If $\phi \simeq \pi$, then $R = -r$ and

$$\mu_p - \mu_b = -\left(\frac{\gamma_b}{D} + \frac{\gamma_s}{r} + p_e - p_p\right)\Omega \ . \tag{31}$$

Obviously $\mu_p - \mu_b < 0$ unless there is an internal pressure, $p_p > 0$, or an external tension, i.e. $-p_e = \overline{\sigma} > 0$. Unless $p_p > 0$ or $\overline{\sigma}$ is sufficiently large, sintering to full density is the equilibrium state.

If $\phi < \phi_c$, then $R > 0$ and $\mu_p = \mu_b = 0$ is possible even with $p_e = p_p = 0$. From Eq. (30) the equilibrium condition for the stress-free case is when

$$\frac{R^*}{D} = \frac{\gamma_s}{\gamma_b} \ , \tag{32}$$

and more generally when

$$\frac{R^*}{D} = \frac{1}{2\cos(\phi/2) - (p_p - p_e)D/\gamma_s} \ , \tag{33}$$

so if the pores are large, $R > R^*$ and they tend to shrink. If the pores are small, $R < R^*$ and they tend to grow. At $R = R^*$ the pore is at a metastable equilibrium. The tendency to growth or shrinkage depends both on the pore curvature which depends on ϕ and N and on the grain size. This is shown in Figure 5 for the stress-free case. Interestingly, for $\phi > 0$ some shrinkage is indicated for all pores.

The question of what occurs when N is very large, Figure 6, is of some interest as $R > 0$ even for quite high ϕ. By considering very large pores it can be shown that

$$\mu_p - \mu_b = \frac{\gamma_b}{D} - \frac{\gamma_s}{R} \simeq \frac{\gamma_s}{r} \ , \tag{34}$$

where r is the radius of the pore. Thus even large pores tend to shrink initially.

From Eq. (15) it is clear that a particular value of R*/D corresponds to a particular porosity. Thus Eqs. (32) and (33) indicate that when $\phi < \phi_c$ there is an "equilibrium" porosity which depends on the number of sides for the pore and on the internal pressure and applied stress. The effect of ϕ and N on the equilibrium porosity, v_f^*, at $p_p = p_e = 0$ is shown in Figure 7. The effect of pressure can be seen from

$$\frac{v_f^*(\bar{\sigma} + p_p)}{v_f^*(0)} = \frac{1}{[1 - (\bar{\sigma} + p_p)D/\gamma_b]^2} , \tag{35}$$

which is plotted in Figure 8.

An interesting result on bloating in the presence of an inert, entrapped gas can be anticipated from Eq. (34) or Figure 8, which show that when the equilibrium porosity results from $p_p > 0$, the relation depends on grain size. The effect can be seen clearly by assuming the gas is ideal, in which case

$$p_p = \frac{n_g kT}{\Sigma V_{pi}} \simeq \frac{n_g kT}{v_f V} . \tag{36}$$

As densification occurs then p_p will increase until $\mu_p - \mu_b = 0$ and densification will stop. This will occur when

$$p_p = \frac{\gamma_b}{D} - \frac{\gamma_s}{R} + p_e = \frac{n_g kT}{v_f V} . \tag{37}$$

Further annealing will result in grain growth and pore growth. If both R and D increase, the equality in Eq. (36) cannot be maintained if the porosity remains constant, i.e., if R/D remains constant. Thus, as R and D increase, v_f must increase which requires that R increases faster than D. This will lead to sintering behavior in which the density goes through a maximum, as shown schematically in Figure 9.

SUMMARY

The thermodynamics for pore growth or shrinkage have been reformulated. The chemical potentials which describe pore growth or shrinkage have terms which depend on the pore curvature, the line tension of the grain boundaries, the applied stress and internal pressure in the pores. The effect of pore curvature may be positive or negative depending on the dihedral angle. The additional grain boundary tension term always favors densification.

The results using a simple model indicate that at low dihedral angle ($\phi < 60°$ in two dimensions, $\phi < 70.5°$ in three dimensions) there is an equilibrium porosity in a polycrystalline material; for such a material there is no barrier to nucleation of cavities in dense material.

At intermediate dihedral angles, pores with few sides would shrink and disappear, whereas those with many sides would initially shrink but would reach an equilibrium size at which densification would stop. In this case grain growth without growth of the large pores would reduce the number of sides for the pore and promote further densification. For such materials there would be a small barrier to nucleation.

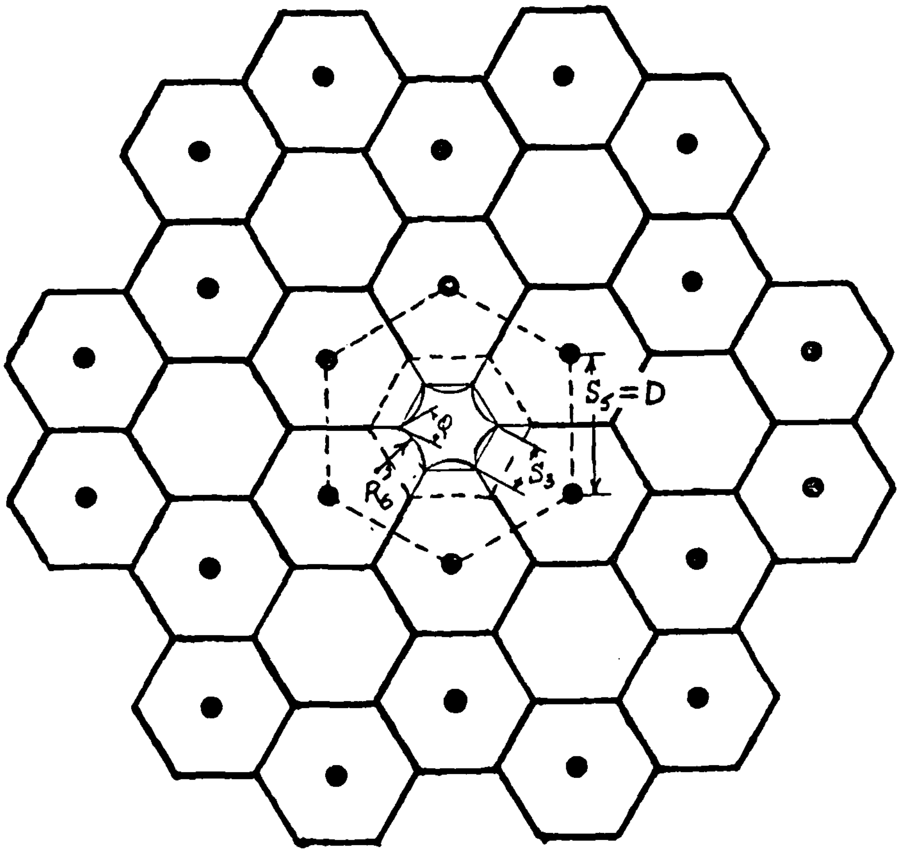

Figure 1. Hexagonal array of grains with only 2/3 of possible grain sites occupied. This can be regarded as a limit of the series of arrays with n'-sided pores and (12-n')-sided grains. Alternatively, it is the limit of stable cells with n grains occupying n+1 sites. The evolution of pore and grain shapes with sintering can be seen in the center pore.

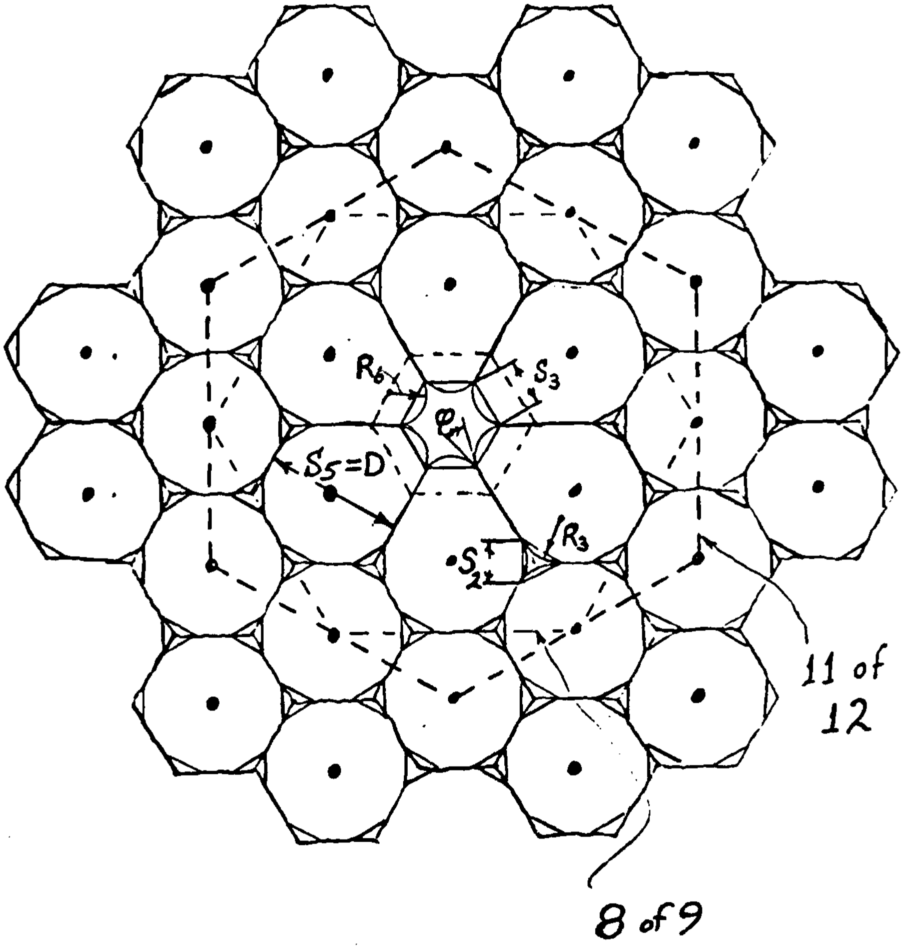
R_6
S_3
φ_1
$S_5 = D$
S_2
R_3
11 of 12
8 of 9

Figure 2. Several cells for arrays of n′ grains occupying n′+1 sites.

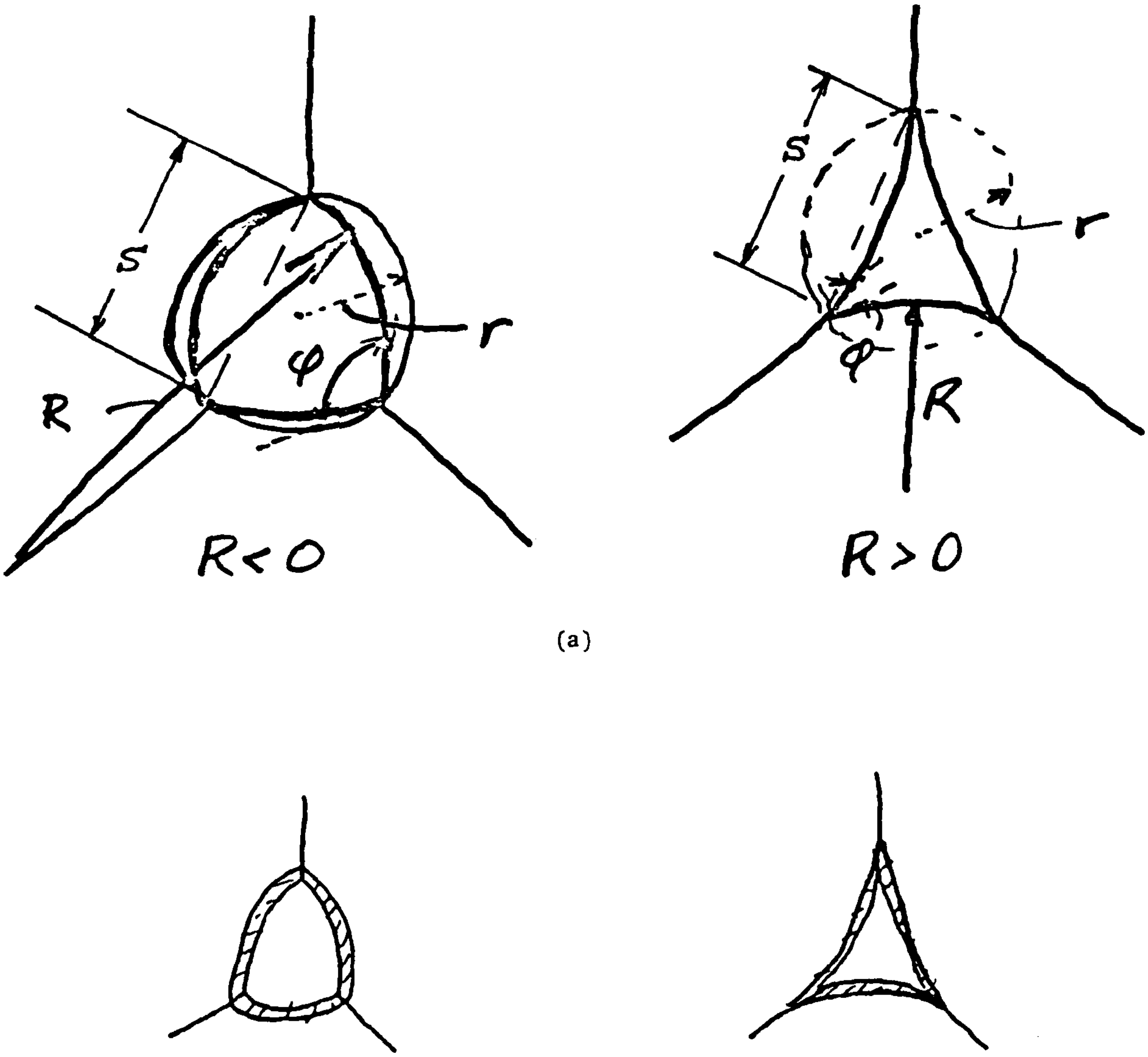

(a)

(b)

Figure 3. The geometry for equilibrium shaped pores is shown in (a) and the effect of adding mass to the pores is indicated schematically in (b).

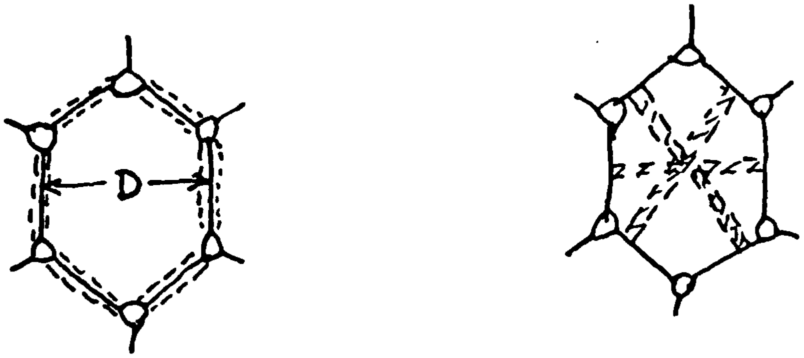

(a)

(b)

Figure 4. Schematic illustration of the effect of adding mass to the grain boundaries where it is distributed uinformly on all grain boundaries within the cell. When all $\delta V_p = 0$, the method of addition in (b) is formally equivalent to mass addition at the boundaries and better illustrates the resulting changes, although it is physically impossible.

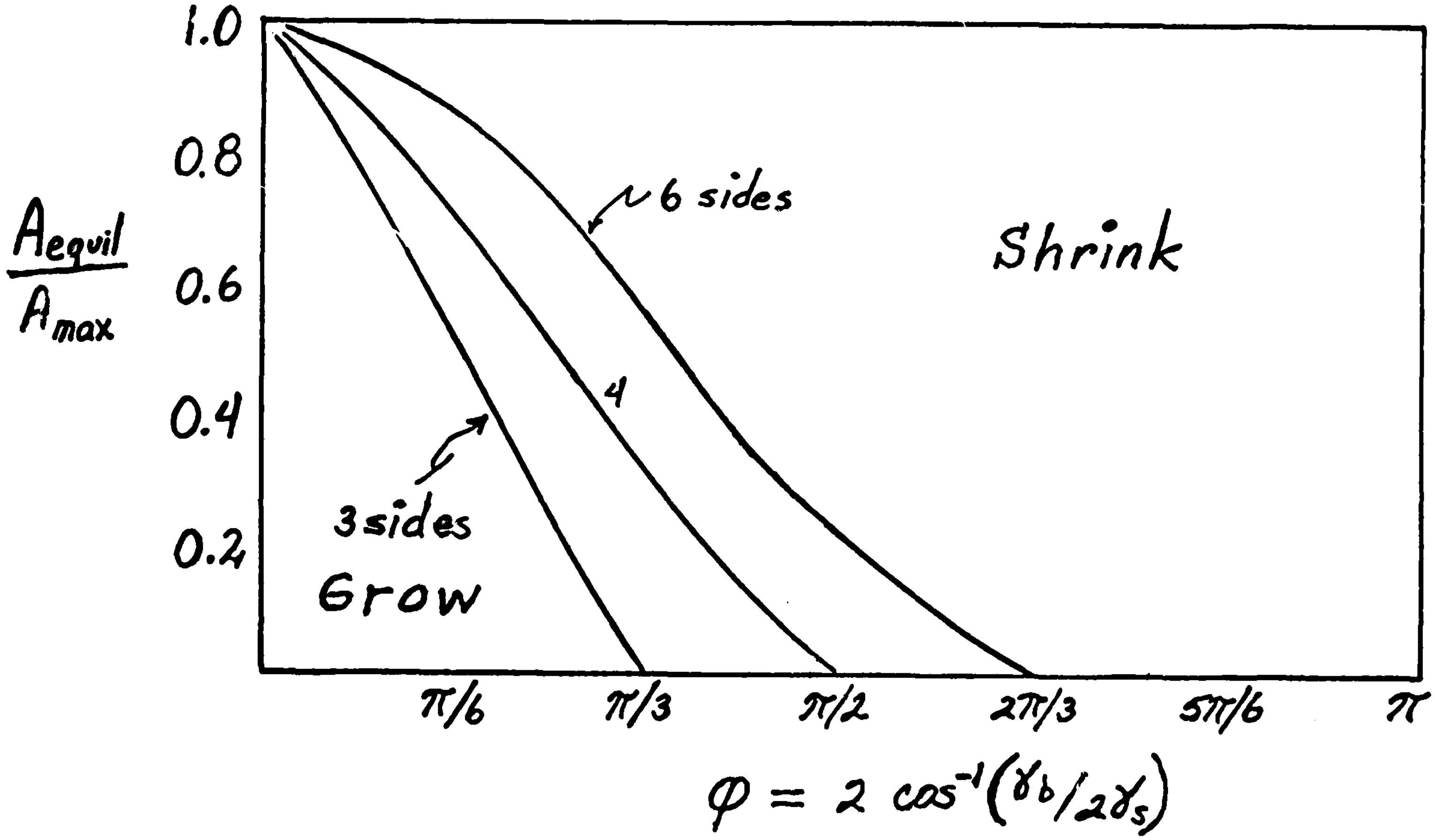

Figure 5. Effect of dihedral angle on the ratio of the equilibrium area of n-sided pores to the maximum area of the pore, that for packing of circles with point contact.

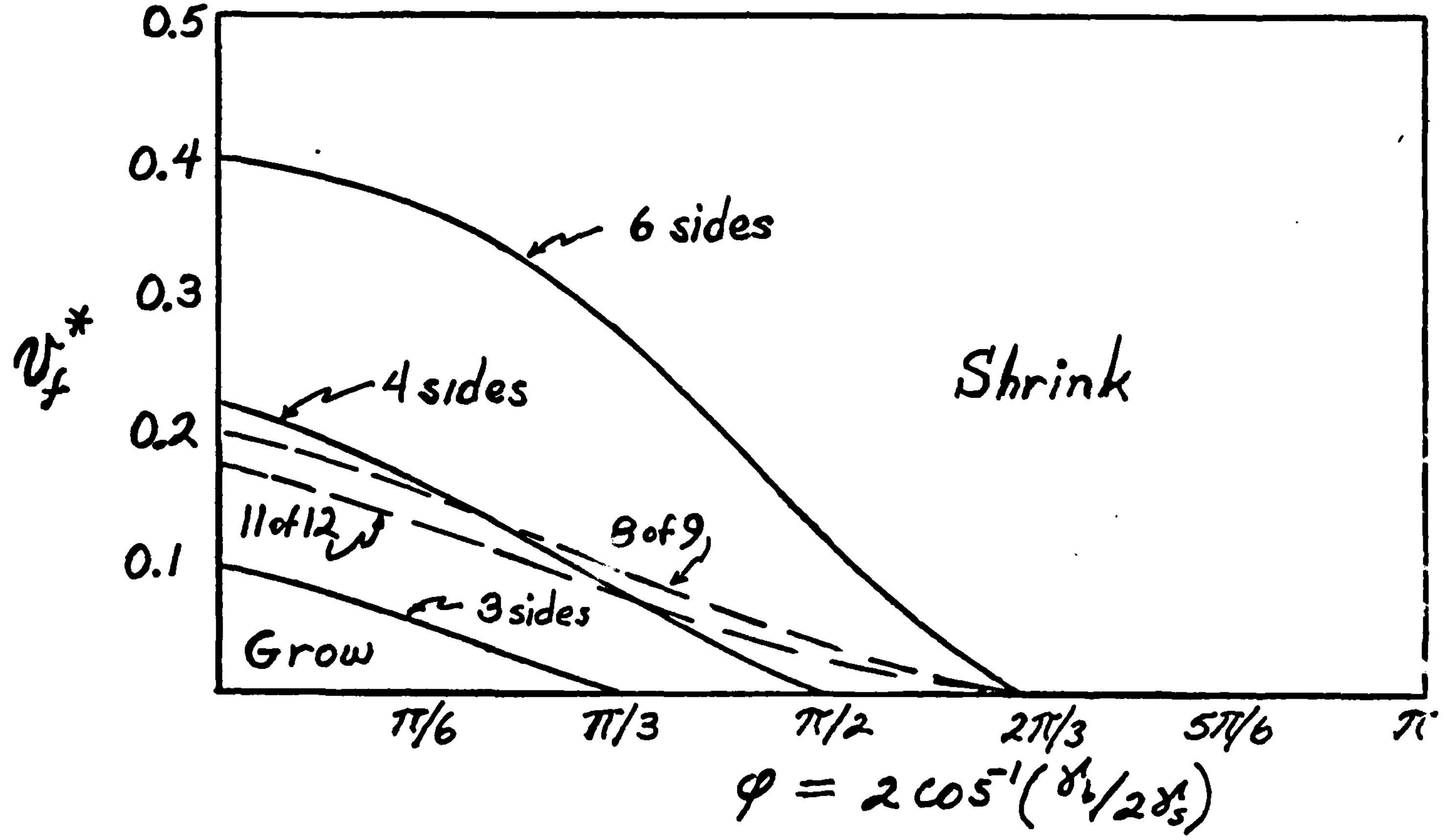

Figure 6. Effect of dihedral angle on the equilibrium porosity for various packing arrangements of circles, and resulting number of sides per pore.

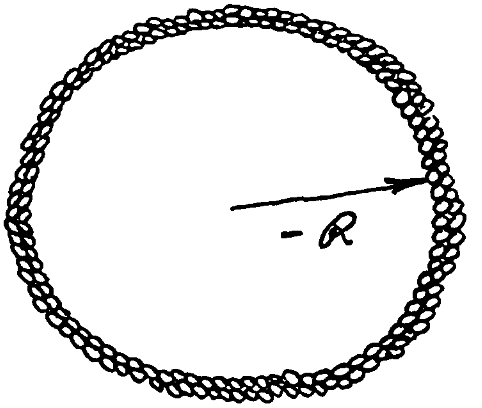

Figure 7. Schematic of a very large pore.

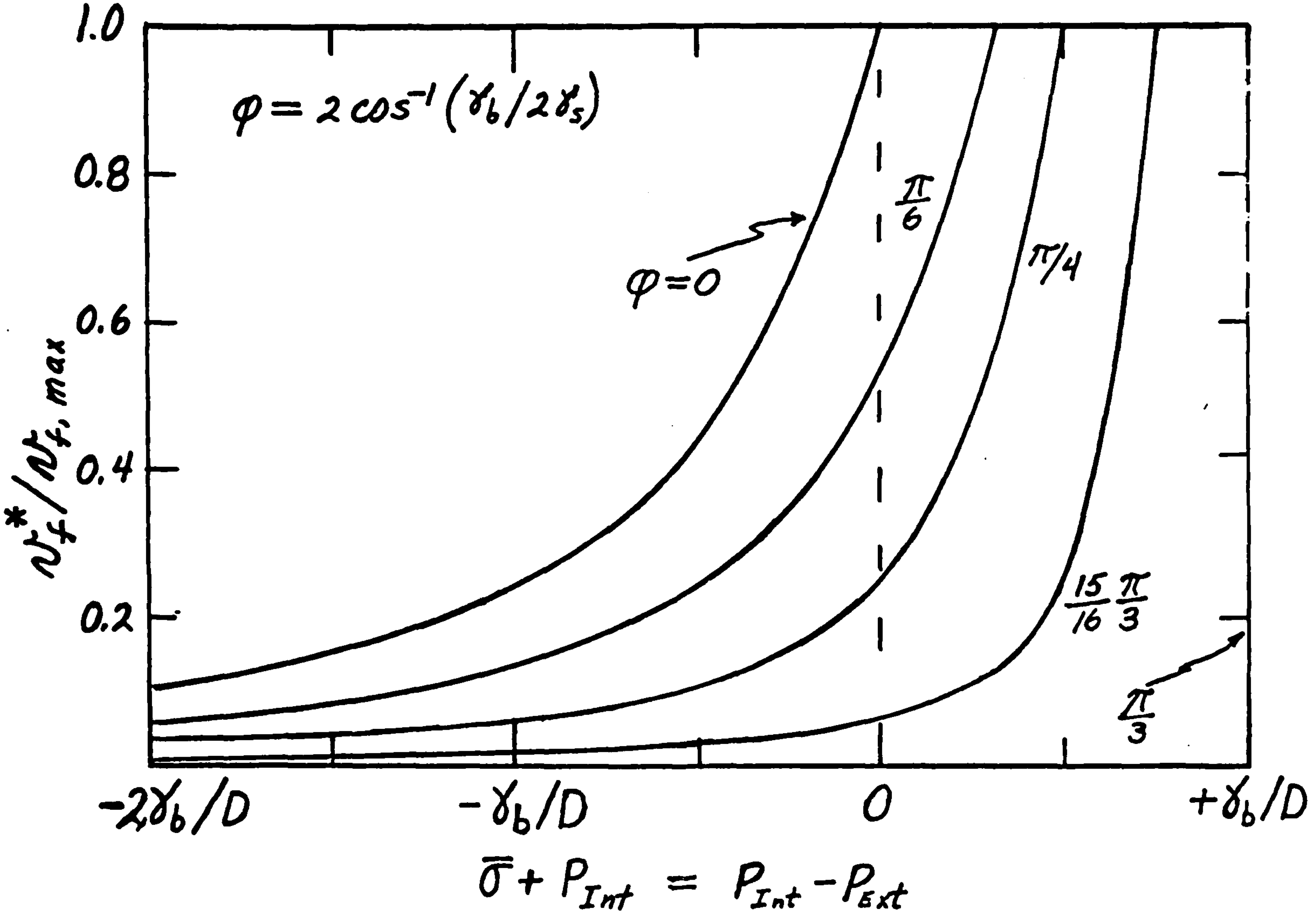

Figure 8. Ratio of the equilibrium porosity to the maximum porosity as a function of applied and internal pressures for various dihedral angles.

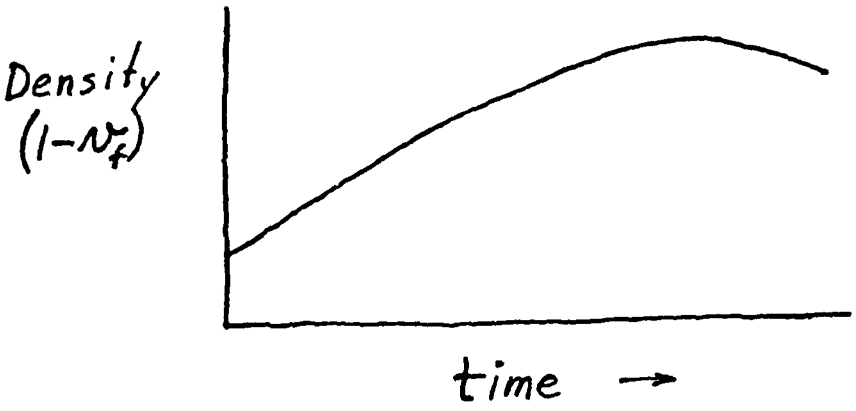

Figure 9. Schematic showing the density go through a maximum with time as a result of sintering and grain growth with an entrapped, insoluble gas in the pores.

END

DATE
FILMED

7-81

DTIC